SIAM J. SCI. COMPUT.
Vol. 40, No. 4, pp. B1020–B1054

AN ARBITRARY-ORDER SCHEME ON GENERIC MESHES FOR MISCIBLE DISPLACEMENTS IN POROUS MEDIA*

DANIEL ANDERSON† AND JÉRÔME DRONIOU†

Abstract. We design, analyze, and implement an arbitrary-order scheme applicable to generic meshes for a coupled elliptic-parabolic PDE system describing miscible displacement in porous media. The discretization is based on several adaptations of the hybrid-high-order (HHO) method due to Di Pietro, Ern, and Lemaire [*Comput. Methods Appl. Math.*, 14 (2014), pp. 461–472]. The equation governing the pressure is discretized using an adaptation of the HHO method for variable diffusion, while the discrete concentration equation is based on the HHO method for advection-diffusion-reaction problems combined with numerically stable flux reconstructions for the advective velocity that we have derived using the results of Cockburn, Di Pietro, and Ern [*ESAIM Math. Model. Numer. Anal.*, 50 (2016), pp. 635–650]. We perform some rigorous analysis of the method to demonstrate its L^2 stability under the irregular data often presented by reservoir engineering problems and present several numerical tests to demonstrate the quality of the results that are produced by the proposed scheme.

Key words. hybrid high-order methods, porous medium, miscible fluid flow, stability analysis, numerical tests

AMS subject classifications. 65M60, 65M12, 65M08

DOI. 10.1137/17M1138807

1. Introduction.

The single-phase flow of incompressible, miscible fluids in a porous medium, arising in the modelling of enhanced oil recovery, is described by a coupled system of nonlinear elliptic-parabolic equations on the pressure and concentration of invading solvent, sometimes referred to as the Peaceman model as derived by Peaceman in [37] (not to be confused with the Peaceman model of wells). Given its complexity, the behavior of this system can only be fully understood through numerical approximations. These approximations must account for the specificities of flows in porous media: discontinuous data, non-Cartesian (and possibly nonconforming) grids, etc.

In this paper, we design an arbitrary-order numerical scheme for the Peaceman model. The stability of the approximation is established, and numerical results are provided. Based on these, we provide advice on how to choose the various parameters of the scheme (spatial order of approximation, time-stepping method, etc.) to optimize the accuracy of the result and the overall computational cost.

Existence of a weak solution to this miscible flow model has been first established in [29], and then extended in [10] to include gravity effects and various boundary conditions. In practice, the molecular diffusion is much smaller than the dispersion effect (driven by the Darcy viscosity), and often neglected in numerical simulation. In that case, the parabolic equation takes on a degenerate form, which makes the analysis of the model even more complex. Amirat and Ziani [1] establish the existence of a

*Submitted to the journal's Computational Methods in Science and Engineering section July 14, 2017; accepted for publication (in revised form) March 5, 2018; published electronically July 10, 2018.

http://www.siam.org/journals/sisc/40-4/M113880.html

Funding: This work was supported by the Australian Government through the Australian Research Council's Discovery Projects funding scheme (project DP170100605), and by Agence Nationale de la Recherche project HHOMM ANR-15-CE40-0005.

†School of Mathematical Sciences, Monash University, Clayton, Victoria 3800, Australia (daniel.anderson@monash.edu, jerome.droniou@monash.edu).

solution in the case of a vanishing molecular diffusion and regular source terms. Given the scale of the reservoir and the well bores, it is customary in simulations to consider wells concentrated on measures (Dirac measures in two dimensions, measures along lines in three dimensions). The corresponding mathematical analysis has been carried out in [22] for nonzero molecular diffusion and in [23] for vanishing molecular diffusion.

A variety of numerical schemes have been considered, with or without convergence analysis, for the Peaceman model. Finite-element based methods coupled with a modified method of characteristic for the advective part of the flow are applied in [26] and analyzed in [27]. Another method of characteristics, the Eulerian–Lagrangian adjoint method, is coupled with $\mathbb{RT}_k$ mixed finite elements (for the pressure) and $\mathbb{Q}_k$ finite elements (for the concentration) in [40, 39]. A method combining $\mathbb{RT}_k$ finite elements and discontinuous Galerkin (dG) schemes is analyzed in [2]. Optimal error estimates for conforming $\mathbb{P}_k$ finite elements on triangles are established in [34], based on maximal regularity properties of the continuous model. Finite-element based methods are natural and well known, but suffer from restrictions on the mesh geometries, which must be conforming and essentially made of triangles or squares. Other schemes have been considered to deal with meshes with generic geometries, as encountered in geophysical applications. In the last few years, schemes have been developed to be applicable on such generic grids. They are mostly based on finite volume techniques, which have the advantage of providing conservative approximations of the Darcy fluxes [19], that can be used in the discretization of the advective terms. In [7], the mixed finite volume (MFV) of [20] is adapted to the Peaceman model, and its convergence analyzed and numerical tests are provided; as shown in [21], this method can be embedded in a larger family, the hybrid mimetic method (HMM) family, that also contains the SUSHI scheme of [28] and the mixed-hybrid mimetic finite difference methods of [6]. Discrete duality finite volume (DDFV) methods are considered in [8, 9]. HMM and DDFV are finite volume schemes with first-order approximation properties and rely for the miscible displacement model on upwinding to stabilize the advective terms; this raises the concern of an overdiffusion of the transition layer between the invading solvent and the residing oil.

In this work, we develop an arbitrary-order numerical scheme for the Peaceman model, which is applicable on generic grids. The scheme is an adaptation of the hybrid high-order (HHO) method, initially developed for stationary diffusion PDEs in [18, 17] and then extended to stationary advection-diffusion-reaction models in [15]. The HHO method can be seen as a higher-order extension of the HMM method, and is very close to virtual element methods [4], to nonconforming mimetic finite difference methods [35], and to hybridizable dG methods [12]. The initial degrees of freedom of the HHO method are scalar valued polynomials of arbitrary-order k on the cells and faces of the mesh. The cell degrees of freedom can however be eliminated by a local static condensation procedure, and only the face degrees of freedom remain coupled, in a way that is however highly parallelizable. The HHO scheme is built on a collection of high-order local reconstruction operators that mimic the quantities present in the weak formulation of the continuous equation. Our executive summary is as follows:

- There is a real advantage in going for a higher-order method. The choice $k = 0$ leads to strong grid effects that are mostly eliminated by taking $k = 1$. This choice $k = 1$ seems to be optimal in terms of accuracy vs. computational cost; the choices $k = 2, 3, \ldots$ increase the computational cost with only minor further improvements of the accuracy.
- A Crank–Nicolson or second-order backward differentiation formula (BDF) time-stepping is sufficient to obtain good results; high-order BDFs tend to

become unstable unless the time-step is reduced a lot, and do not lead to perceptible improvement (even considering higher-order spatial approximation, that is, $k \geq 2$).
- The specific mesh geometry is mostly irrelevant to the quality of the numerical approximation, which mostly seems to only depend on the number of faces of the mesh (which is expected, the face unknowns being the main unknowns in the HHO method).

Let us conclude by describing the organization of the paper. In the next section, we describe the continuous miscible displacement model, both in strong and weak form. The scheme is described in section 3, starting from the time-stepping, designed in a classical way to decouple the pressure and concentration equations. As explained above, the HHO method is built on local polynomial spaces and reconstruction operators; these are, respectively, described in sections 3.2 and 3.3. The discretized pressure equation is then presented. In order to discretize the convection terms appearing in the concentration equation, cell Darcy velocities and corresponding fluxes have to be designed from the numerical solution of the pressure equation. The reconstruction of this velocity and fluxes is described in section 3.5. We note that this reconstruction has to be carefully performed to preserve the scheme stability; in particular, this implies discretizing the pressure equation at an order twice the order chosen for the concentration equation. The numerical approximation of the latter is described in section 3.6. Existence, uniqueness, and stability results for our complete scheme are stated in Theorem 3.7 at the end of section 3. Numerical tests are provided in section 4. We analyze in particular the effect (in terms of cost as well as efficiency) of varying the spatial degree of the method and of having to use distorted polygonal meshes. This analysis is done on test-cases involving homogeneous or discontinuous permeability, with various mesh geometries and by considering both the general eye-ball quality of the solution (compared with the expected behavior), as well as quantitative assessments based on the variation, with respect to the polynomial degrees, of the amount of oil recovered after 10 years. The executive summary above is backed up by the extensive numerical results in this section. A short conclusion is given in section 5, and the proof of the existence, uniqueness, and stability result is given in the first appendix, section 6. These proofs show in particular the importance of choosing, in the discretization of the concentration equation, Darcy velocity and fluxes adapted to the discretization of the pressure equation. A second appendix, section 7, describes the practical implementation of the scheme and provides a link to the code we developed for the numerical tests.

2. The continuous model. We introduce the following notations that will be used to describe the model, and then present the aforementioned system.

$d \in \{2, 3\}$	the number of dimensions considered in the model,
$\Omega \subset \mathbb{R}^d$	a bounded Lipschitz domain representing the reservoir,
$(0, t_f) \subset \mathbb{R}$	the time interval on which we consider the problem,
$p : (0, t_f) \times \Omega \to \mathbb{R}$	the pressure in the mixture,
$\boldsymbol{U} : (0, t_f) \times \Omega \to \mathbb{R}^d$	the Darcy velocity of the fluid,
$c : (0, t_f) \times \Omega \to \mathbb{R}$	the concentration of the invading solvent in the reservoir,
$\hat{c} : (0, t_f) \times \Omega \to \mathbb{R}$	the concentration of solvent as it is injected,
$\Phi : \Omega \to \mathbb{R}$	the porosity of the medium,
$\mu : [0, 1] \to \mathbb{R}$	the viscosity of the fluid mixture at a given concentration,
$\boldsymbol{K} : \Omega \to \mathbb{R}^{d\times d}$	the absolute permeability tensor of the medium,
$\boldsymbol{D} : \Omega \times \mathbb{R}^d \to \mathbb{R}^{d\times d}$	the diffusion-dispersion tensor of the medium,

$q^+ : (0,t_f)\times\Omega \to \mathbb{R}$ the source term corresponding to the injection well,
$q^- : (0,t_f)\times\Omega \to \mathbb{R}$ the source term corresponding to the production well.

Taking the effects of gravity to be negligible, the model reads

$$\begin{cases} \operatorname{div}(\boldsymbol{U}) = q^+ - q^- & \text{in } (0,t_f)\times\Omega, \\ \boldsymbol{U} = -\dfrac{\boldsymbol{K}(x)}{\mu(c)}\nabla p & \text{in } (0,t_f)\times\Omega, \end{cases} \tag{2.1a}$$

$$\Phi(x)\frac{\partial c}{\partial t} - \operatorname{div}(\boldsymbol{D}(x,\boldsymbol{U})\nabla c - c\boldsymbol{U}) + q^- c = q^+\hat{c} \qquad \text{in } (0,t_f)\times\Omega. \tag{2.1b}$$

This system is comprised of two very natural parts. The pressure equation (2.1a) is an anisotropic diffusion equation with diffusivity $-\frac{\boldsymbol{K}}{\mu(c)}$. For simplicity of notation, we may instead write

$$\boldsymbol{\kappa} = \frac{\boldsymbol{K}(x)}{\mu(c)}. \tag{2.1c}$$

The concentration equation (2.1b) describes the convection of the fluid mixture via an advection-diffusion-reaction equation with diffusivity $\boldsymbol{D}$ and advective velocity corresponding to the Darcy velocity of the fluid mixture $\boldsymbol{U}$. We will now briefly summarize the models used for the data. Following [36], Peaceman derived the diffusion-dispersion tensor $\boldsymbol{D}$ to be

$$\boldsymbol{D}(x,\boldsymbol{U}) = \Phi(x)\left(d_m\mathbf{I} + |\boldsymbol{U}|\left(d_l E(\boldsymbol{U}) + d_t(\mathbf{I} - E(\boldsymbol{U}))\right)\right), \tag{2.1d}$$

where d_m is the molecular diffusion coefficient, d_l and d_t are the longitudinal and transverse dispersion coefficients, and $E(\boldsymbol{U})$ is an orthogonal projection in the direction of the Darcy velocity, given by the outer-product

$$E(\boldsymbol{U}) = \frac{\boldsymbol{U}\otimes\boldsymbol{U}}{|\boldsymbol{U}|^2} = \left[\frac{\boldsymbol{U}_i\boldsymbol{U}_j}{|\boldsymbol{U}|^2}\right]_{1\le i,j\le d}. \tag{2.1e}$$

Physical experiments reveal that the longitudinal dispersion d_l is far stronger than the transverse dispersion d_t, and that the molecular dispersion d_m is negligible in comparison [41].

The viscosity of the mixture is determined by the mixing rule given in [32]:

$$\mu(c) = \mu(0)\left(1 + (M^{\frac{1}{4}} - 1)c\right)^{-4}, \qquad c\in[0,1], \tag{2.1f}$$

where $\mu(0)$ is the viscosity of the oil and M is the mobility ratio between the oil and the injected solvent, given by $M = \frac{\mu(0)}{\mu(1)}$.

In order to maintain a balance of mass in the domain, the boundary of the reservoir $\partial\Omega$ is taken to be impermeable. Consequently, we include, denoting by $\mathbf{n}$ the unit exterior normal to $\partial\Omega$, homogeneous no flow Neumann boundary conditions:

$$\begin{cases} \boldsymbol{U}\cdot\mathbf{n} = 0 & \text{on } (0,t_f)\times\partial\Omega, \\ D\nabla c\cdot\mathbf{n} = 0 & \text{on } (0,t_f)\times\partial\Omega. \end{cases} \tag{2.1g}$$

Additionally, in order to satisfy the no flow boundary conditions and maintain mass,

we must further impose that our injection and production source terms are compatible:

$$\int_\Omega q^+(\cdot,x)dx = \int_\Omega q^-(\cdot,x)dx \qquad \text{in } (0,t_f). \tag{2.1h}$$

We must also prescribe an initial condition:

$$c(0,x) = c_0(x). \tag{2.1i}$$

In practice we take the initial concentration in the well to be 0 everywhere. It is also usual to take $\hat{c}$, the concentration at the injection well, to be 1.

Last, since the pressure is only defined up to an arbitrary constant, we normalize p by the following condition:

$$\int_\Omega p(\cdot,x)dx = 0 \qquad \text{in } (0,t_f). \tag{2.1j}$$

2.1. Weak formulation. Noting that the geometry of a typical oil reservoir will contain many geological layers of varying porosity and permeability, it is very important to take into account the fact that these quantities cannot be assumed to be smooth and continuous everywhere. The following assumptions given in [7] are reasonable and allow us to devise both analytically sound and physically acceptable solutions.

$$\begin{gathered}\Phi \in L^\infty(\Omega) \text{ such that there exists } \Phi_* > 0 \text{ satisfying} \\ \Phi_* \le \Phi \le \Phi_*^{-1} \text{ almost everywhere in } \Omega,\end{gathered} \tag{2.2a}$$

$$\begin{gathered}q^+, q^- \in L^\infty(0,t_f;L^2(\Omega)) \text{ are nonnegative and compatible, i.e.,} \\ \int_\Omega q^+(t,x)dx = \int_\Omega q^-(t,x)dx \text{ for almost every } t \in (0,t_f),\end{gathered} \tag{2.2b}$$

$$\begin{gathered}\boldsymbol{K} : \Omega \to M_d(\mathbb{R}) \text{ is a bounded matrix-valued function} \\ \text{admitting symmetric, uniformly coercive values, that is,} \\ \exists \alpha_K > 0 \text{ s.t. } \boldsymbol{K}(x)\xi\cdot\xi \ge \alpha_K|\xi|^2 \text{ for almost every } x \in \Omega \text{ and all } \xi \in \mathbb{R}^d, \\ \exists \Lambda_K > 0 \text{ s.t. } |\boldsymbol{K}(x)| \le \Lambda_K \text{ for almost every } x \in \Omega,\end{gathered} \tag{2.2c}$$

$$\boldsymbol{D} : \Omega \times \mathbb{R}^d \to M_d(\mathbb{R}) \text{ is given by (2.1d) with } d_l, d_m, d_t > 0. \tag{2.2d}$$

$$\begin{gathered}\mu \in \mathcal{C}(\mathbb{R}) \text{ is positively bounded, that is, } 0 \le a \le \mu(c) \le b \text{ for} \\ \text{positive constants } a, b \text{ for all } c \in \mathbb{R}. \text{ This is clearly satisfied by (2.1f),}\end{gathered} \tag{2.2e}$$

$$\begin{gathered}\hat{c} \in L^\infty((0,t_f)\times\Omega) \text{ satisfies } 0 \le \hat{c} \le 1 \text{ almost everywhere,} \\ c_0 \in L^\infty(\Omega) \text{ satisfies } 0 \le c_0 \le 1 \text{ almost everywhere.}\end{gathered} \tag{2.2f}$$

Under the regularity assumptions (2.2), the existence of a weak solution to (2.1a)–(2.1b) is established in [29, 10]. The HHO scheme presented in section 3 consists in discretizing the following equations, satisfied by this weak solution $(p, \boldsymbol{U}, c)$:

$$\begin{cases} p \in L^\infty(0,t_f;H^1(\Omega)),\ \boldsymbol{U} \in L^\infty(0,t_f;L^2(\Omega))^d, \\ c \in \mathcal{C}([0,t_f];L^2(\Omega)) \cap L^2(0,t_f;H^1(\Omega)) \text{ with} \\ \Phi\partial_t c \in L^2(0,t_f;(W^{1,4}(\Omega))') \text{ and } c(0) = c_0, \end{cases} \tag{2.3}$$

$$\begin{cases} \text{for almost every } t \in (0,t_f), \forall \varphi \in H^1(\Omega), \\ -\displaystyle\int_\Omega \boldsymbol{U}(t,\cdot)\cdot\nabla\varphi = \int_\Omega \left(q^+(t,\cdot) - q^-(t,\cdot)\right)\varphi, \end{cases} \tag{2.4}$$

and

$$\text{(2.5)}\qquad \begin{cases} \text{for almost every } t \in (0,t_f),\ \text{for all } \varphi \in W^{1,4}(\Omega), \\ \langle \Phi \partial_t c(t), \varphi \rangle_{(W^{1,4})',W^{1,4}} + \displaystyle\int_\Omega \boldsymbol{D}(\cdot, \boldsymbol{U}(t,\cdot)) \nabla c(t,\cdot) \cdot \nabla \varphi \\ \qquad - \displaystyle\int_\Omega c(t,\cdot) \boldsymbol{U}(t,\cdot) \cdot \nabla \varphi + \int_\Omega q^-(t,\cdot) c(t,\cdot) \varphi = \int_\Omega q^+(t,\cdot) \hat{c}(t) \varphi. \end{cases}$$

3. Numerical scheme. The scheme for the pressure equation consists in the standard HHO method for variable diffusion problems [17], taking into account the coupling of the pressure with the concentration equation. Adapting [12], we derive conservative discrete version of the Darcy velocity and its fluxes that are required to discretize the advective term $\mathrm{div}(\boldsymbol{U}c)$ in the concentration equation. The spatial terms in this equation are discretized by using the HHO method for linear advection-diffusion-reaction [15], incorporating the aforementioned discrete Darcy velocity and fluxes. The time-stepping presented here is based on the Crank–Nicolson method, due to its strong stability properties [33]. (We also tested BDF time-steppings.)

3.1. Time-stepping. We define our time-stepping as follows; let $N \in \mathbb{N}$ be the number of time-steps to be taken and let

$$\text{(3.1)}\qquad \Delta t = \frac{t_f}{N}, \qquad t^n = n\Delta t, \qquad n = 0, 1, \ldots, N.$$

Let us denote the pressure, concentration, and Darcy velocity at time-step n by $p^n = p(t^n,\cdot)$, $c^n = c(t^n,\cdot)$, and $\boldsymbol{U}^n = \boldsymbol{U}(t^n,\cdot) = -\boldsymbol{\kappa}(c^n,\cdot)\nabla p^n$. The Crank–Nicolson time-stepping of (2.1b) consists in writing

$$\text{(3.2)}\qquad \begin{aligned} \Phi(x)\frac{c^{n+1}-c^n}{\Delta t} - \mathrm{div}(D(x,\boldsymbol{U}^{n+1/2})\nabla c^{n+1/2} - c^{n+1/2}\boldsymbol{U}^{n+1/2}) + q^- c^{n+1/2} \\ = q^+ \hat{c}(t^{n+1/2}), \end{aligned}$$

where the intermediate time-stepped values are defined by

$$\text{(3.3)}\qquad \xi^{n+1/2} = \frac{\xi^{n+1}+\xi^n}{2} \qquad (\xi = t,\ c, \text{ or } \boldsymbol{U}).$$

The problem data, e.g., the well terms q^+ and q^-, are evaluated at $t^{n+1/2}$. The formulation (3.2) leads to the following direct relation between c^n and $c^{n+1/2}$:

$$\text{(3.4)}\qquad \begin{aligned} \Phi(x)\frac{2(c^{n+1/2}-c^n)}{\Delta t} - \mathrm{div}(D(x,\boldsymbol{U}^{n+1/2})\nabla c^{n+1/2} - c^{n+1/2}\boldsymbol{U}^{n+1/2}) \\ + q^- c^{n+1/2} = q^+ \hat{c}(t^{n+1/2}). \end{aligned}$$

We note that this formulation is equivalent to performing a half time-step with an implicit Euler scheme to obtain $c^{n+1/2}$ and then linearly extrapolating c^n with $c^{n+1/2}$ to obtain c^{n+1} using (3.3).

3.2. Discretization spaces. Let us briefly introduce the notion of a mesh and define the polynomial spaces central to the scheme.

DEFINITION 3.1. *A mesh $\mathcal{M}$ of $\Omega \subset \mathbb{R}^d$ is a collection of cells and faces $(\mathcal{T},\mathcal{F})$ where the following hold:*

1. *$\mathcal{T}$ (the cells or control volumes) is a subdivision of Ω into a disjoint family of open, nonempty polygons (or polyhedra in higher dimensions). Formally,*

$$\bigcup_{T\in\mathcal{T}} \overline{T} = \overline{\Omega}. \tag{3.5}$$

2. *$\mathcal{F}$ (the faces or edges) is a disjoint family of nonempty affine subsets of Ω with positive $(d-1)$ dimensional measure such that for each cell $T \in \mathcal{T}$, there exists $\mathcal{F}_T \subset \mathcal{F}$, where*

$$\bigcup_{F\in\mathcal{F}_T} \overline{F} = \partial T, \tag{3.6}$$

such that each face $F \in \mathcal{F}$ borders exactly one or two cells.

Additionally, we may employ the following notation.

$\mathcal{F}_T \subset \mathcal{F}$	the faces that border the cell T,
$\mathcal{F}_b \subset \mathcal{F}$	the faces on the boundary of the domain Ω,
$\lvert T\rvert$ or $\lvert F\rvert$	the Lebesgue measure of the cell T or face F,
$\overline{x}_T$	the center of mass of the cell T,
$\mathbf{n}_{TF}$	a normal vector to the face F facing outward from the cell T,
h_T or h_F	the diameter of a cell T or a face F,
$h = \max_{T\in\mathcal{T}} h_T$	the maximum diameter of any cell.

Take $\mathcal{M}_h = (\mathcal{T}_h, \mathcal{F}_h)$ a generic polygonal/polytopal mesh of Ω as above. The degrees of freedom of the scheme are scalar valued polynomials on the cells $T \in \mathcal{T}_h$ and the faces $F \in \mathcal{F}_h$. No continuity conditions between cells and faces, or between cells and cells, are imposed on the degrees of freedom. Selecting an integer $m \geq 0$, the following notation will help us describe the polynomial spaces; here, K is a set of dimension l (that is, the affine space spanned by K has dimension l).

$\mathbb{P}^m(K)$	the space of l-variate polynomials of degree $\leq m$,
$\nabla\mathbb{P}^m(K)$	the space of functions $\{\nabla u : u \in \mathbb{P}^m(K)\}$,
$\pi_K^m : L^2(K) \to \mathbb{P}^m(K)$	the L^2 orthogonal projector onto $\mathbb{P}^m(K)$,

where the L^2 orthogonal projector is given by:

$$\pi_K^m(u) = v \in \mathbb{P}^m(K) \text{ is such that, } \forall w \in \mathbb{P}^m(K), \int_K (u-v)w = 0. \tag{3.7}$$

The spaces of degrees of freedom are then given as follows.

Definition 3.2. *Let $\mathcal{M}_h$ be a mesh. For each cell $T \in \mathcal{T}_h$, the space of local degrees of freedom on T is defined by*

$$X_T^m = \mathbb{P}^m(T) \times \left\{ \bigtimes_{F\in\mathcal{F}_T} \mathbb{P}^m(F) \right\}. \tag{3.8}$$

The space of global degrees of freedom on the mesh is defined as

$$X_h^m = \left\{ \bigtimes_{T\in\mathcal{T}_h} \mathbb{P}^m(T) \right\} \times \left\{ \bigtimes_{F\in\mathcal{F}_h} \mathbb{P}^m(F) \right\}. \tag{3.9}$$

For a given $k \geq 0$, these spaces will be used to approximate both the pressure (with $m = 2k$) and the concentration (with $m = k$). An arbitrary set of global degrees of freedom is denoted by

$$\underline{\mathrm{u}}_h = ((\mathrm{u}_T)_{T\in\mathcal{T}_h}, (\mathrm{u}_F)_{F\in\mathcal{F}_h}) \in X_h^m, \tag{3.10}$$

and, similarly, a set of local degrees of freedom is

$$\underline{\mathrm{u}}_T = (\mathrm{u}_T, (\mathrm{u}_F)_{F\in\mathcal{F}_T}) \in X_T^m. \tag{3.11}$$

For a given $\underline{\mathrm{u}}_h \in X_h^m$, we define $\mathrm{u}_h \in L^2(\Omega)$ as the piecewise polynomial function given by $(\mathrm{u}_h)_{|T} = \mathrm{u}_T$ for all $T \in \mathcal{T}_h$. The space of degrees of freedom with zero average is then

$$X_{h,*}^m = \left\{ \underline{\mathrm{u}}_h \in X_h^m \,:\, \int_\Omega \mathrm{u}_h = 0 \right\}. \tag{3.12}$$

3.3. Reconstruction operators. We now introduce the local reconstruction operators which are central to the scheme. The cornerstone of the HHO method is a high-order local gradient reconstruction operator based on the cell and face polynomial degrees of freedom.

DEFINITION 3.3. *Let $\mathbf{\Lambda}$ be a bounded, real, symmetric, coercive tensor-valued function on Ω. Take a cell $T \in \mathcal{T}_h$ of $\mathcal{M}$. The local reconstruction operator $\boldsymbol{r}_{T,\mathbf{\Lambda}}^{m+1} : X_T^m \to \mathbb{P}^{m+1}(T)$ is defined such that, for a bundle of local degrees of freedom $\underline{\mathrm{u}}_T = (\mathrm{u}_T, (\mathrm{u}_F)_{F\in\mathcal{F}_T}) \in X_T^m$ and any test function $w \in \mathbb{P}^{m+1}(T)$,*

$$\int_T \mathbf{\Lambda}\nabla \boldsymbol{r}_{T,\mathbf{\Lambda}}^{m+1}\underline{\mathrm{u}}_T \cdot \nabla w = \int_T \mathbf{\Lambda}\nabla \mathrm{u}_T \cdot \nabla w + \sum_{F\in\mathcal{F}_T} \int_F (\mathrm{u}_F - \mathrm{u}_T)\nabla w \cdot (\mathbf{\Lambda}\mathbf{n}_{TF}), \tag{3.13}$$

and

$$\int_T \boldsymbol{r}_{T,\mathbf{\Lambda}}^{m+1}\underline{\mathrm{u}}_T = \int_T \mathrm{u}_T. \tag{3.14}$$

In addition to the local reconstruction operator, we define the local high-order correction operator.

DEFINITION 3.4. *The high-order correction operator $\boldsymbol{R}_{T,\mathbf{\Lambda}}^{m+1} : X_T^m \to \mathbb{P}^{m+1}(T)$ is defined such that*

$$\boldsymbol{R}_{T,\mathbf{\Lambda}}^{m+1}\underline{\mathrm{u}}_T = \mathrm{u}_T + (\boldsymbol{r}_{T,\mathbf{\Lambda}}^{m+1}\underline{\mathrm{u}}_T - \pi_T^m \boldsymbol{r}_{T,\mathbf{\Lambda}}^{m+1}\underline{\mathrm{u}}_T). \tag{3.15}$$

We remark that the bracketed term of (3.15) *is orthogonal to $\mathbb{P}^m(T)$ by construction, and hence this operator can be seen as adding a high-order orthogonal correction to the cell unknown $\mathrm{u}_T \in \mathbb{P}^m(T)$.*

3.4. The pressure equation. Let us fix an integer $k \geq 0$. The HHO scheme for (2.1) consists in discretizing the pressure in X_h^{2k} and the concentration in X_h^k. The choice of an order $2k$, instead of k, for the pressure is driven by stability considerations, which are made clear in the proof of Theorem 3.7 (see Remark 6.3).

To write the scheme on the pressure, we introduce the following local bilinear forms: $a_{T,\mathbf{\Lambda}} : X_T^{2k} \times X_T^{2k} \to \mathbb{R}$ and $s_{\mathbf{\Lambda},T} : X_T^{2k} \times X_T^{2k} \to \mathbb{R}$, defined by

$$a_{T,\mathbf{\Lambda}}(\underline{\mathrm{u}}_T, \underline{\mathrm{w}}_T) = \int_T \mathbf{\Lambda}\nabla \boldsymbol{r}_{T,\mathbf{\Lambda}}^{2k+1}\underline{\mathrm{u}}_T \cdot \nabla \boldsymbol{r}_{T,\mathbf{\Lambda}}^{2k+1}\underline{\mathrm{w}}_T + s_{\mathbf{\Lambda},T}(\underline{\mathrm{u}}_T, \underline{\mathrm{w}}_T), \tag{3.16}$$

$$s_{\mathbf{\Lambda},T}(\underline{\mathrm{u}}_T, \underline{\mathrm{w}}_T) = \sum_{F\in\mathcal{F}_T} \frac{\mathbf{\Lambda}_{TF}}{h_F} \int_F \pi_F^{2k}(\mathrm{u}_F - \boldsymbol{R}_{T,\mathbf{\Lambda}}^{2k+1}\underline{\mathrm{u}}_T)\pi_F^{2k}(\mathrm{w}_F - \boldsymbol{R}_{T,\mathbf{\Lambda}}^{2k+1}\underline{\mathrm{w}}_T), \tag{3.17}$$

where

$$\boldsymbol{\Lambda}_{TF} = \|\mathbf{n}_{TF} \cdot \boldsymbol{\Lambda}_{|T} \mathbf{n}_{TF}\|_{L^\infty(F)} \tag{3.18}$$

is a controlling factor for the size of $\boldsymbol{\Lambda}$ (in cell T) across the face F. The first term of $a_{T,\boldsymbol{\Lambda}}$ can readily be recognized as a discrete analogue of the weak diffusive terms of the weak formulation. The function $s_{\boldsymbol{\Lambda},T}$ is the diffusive stabilization term whose purpose is to enforce a least-squares penalty between face unknowns, and the projection of the high-order correction of the cell unknown. This is required to ensure that the cell and face unknowns are related, and to ensure that the global bilinear form defined in (3.19) below is symmetric positive definite on $X_{h,*}^{2k}$ (see Lemma 6.1).

Finally we can define the global pressure bilinear form that mimics the weak pressure equation (2.4). We denote by $a_{h,\boldsymbol{\Lambda}} : X_h^{2k} \times X_h^{2k} \to \mathbb{R}$ the global bilinear form such that

$$a_{h,\boldsymbol{\Lambda}}(\underline{\mathrm{u}}_h, \underline{\mathrm{w}}_h) = \sum_{T \in \mathcal{T}_h} a_{T,\boldsymbol{\Lambda}}(\underline{\mathrm{u}}_T, \underline{\mathrm{w}}_T). \tag{3.19}$$

We also write the linear functional $l_h^{p,n+1/2} : X_h^{2k} \to \mathbb{R}$ such that

$$l_h^{p,n+1/2}(\underline{\mathrm{w}}_h) = \int_\Omega (q^+(t^{n+1/2}, \cdot) - q^-(t^{n+1/2}, \cdot))\mathrm{w}_h, \tag{3.20}$$

which mimics the right-hand side of the weak pressure equation.

Recalling that the pressure equation has diffusion tensor $\boldsymbol{\Lambda} = \boldsymbol{\kappa}(c)$ given by (2.1c), the discrete pressure $\underline{\mathrm{p}}_h^{n+1/2} \in X_{h,*}^{2k}$ on $[t^n, t^{n+1})$ is computed by solving

$$a_{h,\boldsymbol{\kappa}^{n+1/2}}(\underline{\mathrm{p}}_h^{n+1/2}, \underline{\mathrm{w}}_h) = l_h^{p,n+1/2}(\underline{\mathrm{w}}_h) \qquad \forall \underline{\mathrm{w}}_h \in X_{h,*}^{2k}, \tag{3.21}$$

where $\boldsymbol{\kappa}^{n+1/2} = \boldsymbol{\kappa}(\tilde{\mathrm{c}}^{n+1/2})$ with $\tilde{\mathrm{c}}^{n+1/2}$ the following extrapolation of the concentration at time $t^{n+1/2}$:

$$\tilde{\mathrm{c}}^{n+1/2} = \frac{3}{2}\mathrm{c}^n - \frac{1}{2}\mathrm{c}^{n-1}. \tag{3.22}$$

(We take $\mathrm{c}_T^{-1} = \mathrm{c}_T^0 = \pi_T^k c_0$ for all $T \in \mathcal{T}_h$.) Note that this choice of extrapolation decouples the pressure equation from the concentration equation (see Algorithm 1 below). Of course, (3.21) only defines the pressure up to an additive constant, so we normalize by imposing

$$\int_\Omega \mathrm{p}_h^{n+1/2} = 0. \tag{3.23}$$

3.5. The discrete fluxes. As can be readily seen from the concentration equation (2.1b), the distribution of the concentration depends heavily on the Darcy velocity of the invading fluid as defined by the pressure equation (2.1a). In the HHO framework, the discretization of advective terms is done by using both the velocity in each cell and its fluxes through the faces [15]. This velocity and fluxes must be properly chosen to ensure the numerical stability of the discretized concentration equation—the fact that $\mathrm{div}(\boldsymbol{U}) = q^+ - q^-$ at the continuous level is what ensures stability estimates on the continuous concentration, and this must be mimicked at the discrete level.

For simplicity of notation, we let here $\underline{\mathrm{p}}_h = \underline{\mathrm{p}}_h^{n+1/2}$ and $\boldsymbol{\kappa} = \boldsymbol{\kappa}^{n+1/2}$. Define $\boldsymbol{\kappa}_{TF}$ from $\boldsymbol{\kappa}$ by (3.18). Following [12, section 3.1], the numerical flux U_{TF}, outward from cell T through the face F, is given by

$$\mathrm{U}_{TF} = -\boldsymbol{\kappa}\nabla \boldsymbol{r}_{T,\boldsymbol{\kappa}}^{2k+1}\underline{\mathrm{p}}_T \cdot \mathbf{n}_{TF} + \frac{\boldsymbol{\kappa}_{TF}}{h_F} s_{\partial T}^{2k,\dagger}\left(\pi_F^{2k}(\boldsymbol{R}_{T,\boldsymbol{\kappa}}^{2k+1}\underline{\mathrm{p}}_T - \mathrm{p}_F)\right), \tag{3.24}$$

where, setting $X_{\partial T}^{2k} = \bigtimes_{F\in\mathcal{F}_T}\mathbb{P}^{2k}(F)$ (identified with a subspace of $L^2(\partial T)$), $s_{\partial T}^{2k,\dagger}$ is the adjoint, for the $L^2(\partial T)$ inner product, of the operator $s_{\partial T}^{2k} : X_{\partial T}^{2k} \to X_{\partial T}^{2k}$ defined by the following: for all $\underline{\mathrm{w}}_{\partial T} = (\mathrm{w}_F)_{F\in\mathcal{F}_T} \in X_{\partial T}^{2k}$,

$$s_{\partial T}^{2k}(\underline{\mathrm{w}}_{\partial T}) = \left(\pi_F^{2k}[\mathrm{w}_F - \boldsymbol{r}_{T,\boldsymbol{\kappa}}^{2k+1}(0,\underline{\mathrm{w}}_{\partial T}) + \pi_T^{2k}\boldsymbol{r}_{T,\boldsymbol{\kappa}}^{2k+1}(0,\underline{\mathrm{w}}_{\partial T})]\right)_{F\in\mathcal{F}_T}. \tag{3.25}$$

The first term of (3.24) can be seen as the "naive" discrete flux that we would obtain if we simply substituted the discrete pressure into the definition of the continuous fluxes. The second term can thus be thought of as a discrete conservative correction to the naive flux.

The discrete Darcy velocity in cell T is then given by

$$\mathbf{U}_T = -\boldsymbol{\kappa}\nabla r_{T,\boldsymbol{\kappa}}^{2k+1}\underline{\mathrm{p}}_T. \tag{3.26}$$

Finally, it is important to note that the discrete fluxes and Darcy velocity satisfy the following local conservation condition from [12].

THEOREM 3.5. *Let $T \in \mathcal{T}_h$ and let $\underline{\mathrm{p}}_h$ be the solution to* (3.21)*. Then for any $\underline{\mathrm{w}}_T \in X_T^{2k}$, the discrete Darcy velocity and fluxes* (3.24) *satisfy*

$$a_{T,\boldsymbol{\kappa}}(\underline{\mathrm{p}}_T,\underline{\mathrm{w}}_T) = -\int_T \mathbf{U}_T\cdot\nabla\mathrm{w}_T + \sum_{F\in\mathcal{F}_T}\int_F \mathrm{U}_{TF}(\mathrm{w}_T - \mathrm{w}_F). \tag{3.27}$$

3.6. Concentration equation. The discrete concentration equation is formulated in terms of a stationary advection-diffusion-reaction equation as in [15], with source and reaction terms incorporating the time-stepping. We recall that, for the concentration equation, the relevant discrete space is X_h^k.

We consider $\mathbf{U} = ((\mathbf{U}_T)_{T\in\mathcal{T}_h}, (U_{TF})_{T\in\mathcal{T}_h, F\in\mathcal{F}_T})$ the Darcy velocity and fluxes reconstructed above at time $t^{n+1/2}$. The following discrete advective derivative $\mathcal{G}_{T,\mathbf{U}}^k\underline{\mathrm{v}}_T$ is designed to be a high-order approximation to the continuous quantity $\boldsymbol{U}\cdot\nabla v$ on the cell T.

DEFINITION 3.6. *For all $T \in \mathcal{T}_h$, the discrete advective derivative $\mathcal{G}_{T,\mathbf{U}}^k : X_T^k \to \mathbb{P}^k(T)$ is such that, for any $\underline{\mathrm{v}}_T \in X_T^k$ and any test function $w \in \mathbb{P}^k(T)$,*

$$\int_T (\mathcal{G}_{T,\mathbf{U}}^k\underline{\mathrm{v}}_T)w = \int_T (\mathbf{U}_T\cdot\nabla\mathrm{v}_T)w + \sum_{F\in\mathcal{F}_T}\int_F \mathrm{U}_{TF}(\mathrm{v}_F - \mathrm{v}_T)w. \tag{3.28}$$

Recalling Definition (2.1d), we define the discrete reconstructed diffusion tensor $\mathbf{D}$ for each cell $T \in \mathcal{T}_h$ for any $x \in T$ by

$$\mathbf{D}(x) = \Phi(x)(d_m\mathbf{I} + |\mathbf{U}_T(x)|(d_l E(\mathbf{U}_T(x)) + d_t(\mathbf{I} - E(\mathbf{U}_T(x))))). \tag{3.29}$$

The local advection-reaction bilinear form $a_{T,R,\mathbf{U}} : X_h^k \times X_h^k \to \mathbb{R}$ is then defined as

$$a_{T,R,\mathbf{U}}(\underline{\mathrm{u}}_T,\underline{\mathrm{w}}_T) = -\int_T \mathrm{u}_T(\mathcal{G}_{T,\mathbf{U}}^k\underline{\mathrm{w}}_T) + \int_T R\mathrm{u}_T\mathrm{w}_T + s_{T,\mathbf{U}}(\underline{\mathrm{u}}_T,\underline{\mathrm{w}}_T), \tag{3.30}$$

where R are the reaction terms, encompassing the time-stepping, given by

$$R = \frac{2\Phi}{\Delta t} + q^-(t^{n+1/2}, \cdot). \tag{3.31}$$

Furthermore, $s_{T,\mathbf{U}} : X_T^k \times X_T^k \to \mathbb{R}$ is the advective stabilization term given by

$$s_{T,\mathbf{U}}(\underline{\mathrm{u}}_T, \underline{\mathrm{w}}_T) = \sum_{F \in \mathcal{F}_T} \int_F [\mathrm{U}_{TF}]^-(\mathrm{u}_F - \mathrm{u}_T)(\mathrm{w}_F - \mathrm{w}_T), \tag{3.32}$$

where $[\mathrm{U}_{TF}]^- = \max(0, -\mathrm{U}_{TF})$. The global advection-reaction bilinear form $a_{h,R,\mathbf{U}} : X_h^k \times X_h^k \to \mathbb{R}$ is defined such that

$$a_{h,R,\mathbf{U}}(\underline{\mathrm{u}}_h, \underline{\mathrm{w}}_h) = \sum_{T \in \mathcal{T}_h} a_{T,R,\mathbf{U}}(\underline{\mathrm{u}}_T, \underline{\mathrm{w}}_T). \tag{3.33}$$

Combining the diffusion and advection-reaction bilinear forms, the complete bilinear form for advection-diffusion-reaction is $a_{h,\mathbf{D},R,\mathbf{U}} : X_h^k \times X_h^k \to \mathbb{R}$ such that

$$a_{h,\mathbf{D},R,\mathbf{U}}(\underline{\mathrm{u}}_h, \underline{\mathrm{w}}_h) = a_{h,\mathbf{D}}(\underline{\mathrm{u}}_h, \underline{\mathrm{w}}_h) + a_{h,R,\mathbf{U}}(\underline{\mathrm{u}}_h, \underline{\mathrm{w}}_h),$$

and the global linear functional $l_h^{c,n+1/2} : X_h^k \to \mathbb{R}$ is

$$l_h^{c,n+1/2}(\underline{\mathrm{w}}_h) = \int_\Omega \left(q^+(t^{n+1/2}, \cdot)\hat{c}(t^{n+1/2}, \cdot) + \frac{2\Phi}{\Delta t}\mathrm{c}_h^n \right) \mathrm{w}_h. \tag{3.34}$$

The discrete concentration scheme then consists in seeking $\underline{\mathrm{c}}_h^{n+1/2} \in X_h^k$ such that

$$a_{h,\mathbf{D},R,\mathbf{U}}(\underline{\mathrm{c}}_h^{n+1/2}, \underline{\mathrm{w}}_h) = l_h^{c,n+1/2}(\underline{\mathrm{w}}_h) \qquad \forall \underline{\mathrm{w}}_h \in X_h^k, \tag{3.35}$$

then extrapolating to obtain $\underline{\mathrm{c}}_h^{n+1}$. We recall that $\mathbf{D}$ and $\mathbf{U}$ are computed from $\underline{\mathrm{p}}_h^{n+1/2}$, and therefore depend on n.

The full scheme is summarized in Algorithm 1.

Algorithm 1 Complete scheme for the pressure-concentration.

1: Set $\mathrm{c}_T^{-1} = \mathrm{c}_T^0 = \pi_T^k c_0$ for all $T \in \mathcal{T}_h$
2: **for** $n = 0$ to $N - 1$ **do**
3: Compute $\underline{\mathrm{p}}_h^{n+1/2}$ by (3.21)–(3.23) from c_h^{n-1} and c_h^n.
4: Compute $\mathbf{U}$ by (3.24) and (3.26) with $\underline{\mathrm{p}}_h = \underline{\mathrm{p}}_h^{n+1/2}$.
5: Compute $\underline{\mathrm{c}}_h^{n+1/2}$ by (3.35) and set $\underline{\mathrm{c}}_h^{n+1} = 2\underline{\mathrm{c}}_h^{n+1/2} - \underline{\mathrm{c}}_h^n$.
6: **end for**

At each iteration, $(\underline{\mathrm{p}}_h^{n+1/2}, \underline{\mathrm{c}}_h^{n+1/2})$ are computed by solving two decoupled linear equations, one corresponding to an HHO scheme for a pure diffusion equation, the other one to an HHO scheme for a diffusion-advection-reaction equation.

Essential questions when designing a numerical scheme are the existence, uniqueness, and stability of its solution; here, stability is understood as the grid size and time-steps go to zero. The following theorem brings an answer to these questions. It states the existence and uniqueness of the solution to the scheme and provides a

bound on the cell unknowns corresponding to the concentration. We note that this bound is, of course, uniform with respect to the grid size, but also with respect to other important parameters, in particular the molecular, longitudinal, and transverse dispersion coefficients d_m, d_l, and d_t. A stability with respect to d_m is all the more essential since this coefficient tends to be taken equal to 0 in numerical tests [40, 7].

THEOREM 3.7 (existence, uniqueness, and estimates for the discrete solution). *Let $\mathcal{M} = (\mathcal{T}_h, \mathcal{F}_h)$ be a mesh of Ω and take $N \geq 1$. If $(q^+, q^-, \boldsymbol{K}, \boldsymbol{D}, \Phi, \hat{c}, c_0)$ are data satisfying (2.2), then there exists a unique solution $(\underline{\mathrm{p}}_h, \underline{\mathrm{c}}_h)$ to the iterative scheme described in Algorithm 1. Morever, for all $n = 0, \ldots, N$,*

$$\|\mathrm{c}_h^n\|_{L^2(\Omega)}^2 \leq \frac{e^2}{\Phi_*^2} \left(\|\mathrm{c}_h^0\|_{L^2(\Omega)}^2 + 2t_f^2 \|q^+\|_{L^\infty(0,t_f;L^2(\Omega))}^2 \right). \tag{3.36}$$

The proof of Theorem 3.7 is provided in the appendix.

4. Tests. In this section, we illustrate the results obtained from the HHO scheme for the simulation of miscible fluid displacement in an oil reservoir. Some of the following test cases first appeared in [38] for the ELLAM-MFEM method and have been subsequently applied in [7] for the MFV scheme. In every simulation here, we use the spatial domain $\Omega = (0, 1000)^2$ measured in ft^2 and consider the time period $[0, 3600]$ (approximately 10 years) measured in days. The injection and production source terms are Dirac masses, approximated as usual by a piecewise constant function on the relevant mesh cells. The injection well is located at $(1000, 1000)$ with an injection rate of 30 ft^2/day. The production well is correspondingly located at $(0, 0)$ with a production rate of 30 ft^2/day. We always take the injected concentration $\hat{c} = 1$ with an initial condition given by $c_0(x) = 0$. The viscosity of the oil is given by $\mu(0) = 1.0$ cp and the mobility ratio is $M = 41$ (see (2.1f)). We assume that molecular diffusion is negligible, setting $d_m = 0.0$ ft^2/day contrasting with the dispersion effects $d_l = 50.0$ ft^2/day and $d_t = 5.0$ ft^2/day. The porosity of the medium is taken to be a constant $\Phi(x) = 0.1$. For each test we present surface and contour plots of the concentration c, the principle quantity of interest.

All tests were run on a laptop with processor Intel i7-4710MQ 2.5Ghz, 6MB cache, and 16GB of RAM at 1600Mhz.

Remark 4.1. Taking $d_m > 0$ is required to meet the regularity assumptions (2.2) but is physically unrealistic due to the fact that the magnitude of the molecular diffusion present in miscible fluid flow is negligibly small compared to the dispersive effects. We will present results taking $d_m = 0$ to demonstrate the suitability of the scheme to real-world parameters. We recall that the stability result of Theorem 3.7 is independent of d_m and is therefore uniformly valid up to the limit $d_m \to 0$.

Tables 1 and 2 give the numbers of edges and sizes (maximum ratio of area to perimeter across all cells) for each mesh used in the following tests. The four mesh varieties are shown in Figure 1. The triangular, Cartesian, and Kershaw meshes were first introduced in the FVCA5 benchmark [30] as mesh families 1, 2, and 4.1, respectively. The hexagonal-dominant mesh was used in [5, 13].

4.1. Numerical results. In these first four tests, we use a polynomial degree $k = 1$ for the spatial discretization. The time-step is $\Delta t = 18$ days ($N \approx 200$ time-steps over 10 years).

TEST 4.1.1. *We take a homogeneous permeability tensor $\boldsymbol{K} = 80\boldsymbol{I}$ uniformly over the domain. We experiment on a 32×32 Cartesian mesh (Cartesian Mesh 4 in*

TABLE 1
Mesh parameters for the meshes used in homogeneous permeability tests.

Number of edges				
	Triangular	Cartesian	Kershaw	Hexagonal
Mesh 1	92	40	612	62
Mesh 2	352	144	2380	220
Mesh 3	1376	544	5304	824
Mesh 4	5540	2112	9384	3184
Mesh 5	21632	8320	14620	12512
Mesh size				
	Triangular	Cartesian	Kershaw	Hexagonal
Mesh 1	31.8	62.5	16.2	70.6
Mesh 2	15.9	31.2	8.96	36.7
Mesh 3	7.95	15.6	6.12	18.5
Mesh 4	3.98	7.81	4.64	9.26
Mesh 5	1.99	3.91	3.73	4.63

TABLE 2
Mesh parameters for the meshes used in discontinuous permeability tests.

Number of edges		
	Triangular	Cartesian
Mesh 1	545	144
Mesh 2	2140	840
Mesh 3	4785	1860
Mesh 4	8480	3280
Mesh 5	13225	5100
Mesh size		
	Triangular	Cartesian
Mesh 1	12.72	31.25
Mesh 2	6.36	12.5
Mesh 3	4.24	8.33
Mesh 4	3.18	6.25
Mesh 5	2.54	5.00

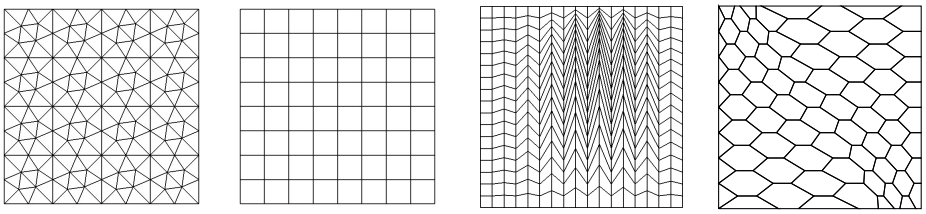

(a) Triangular. (b) Cartesian. (c) Kershaw. (d) Hexagonal.

FIG. 1. *The four varieties of meshes. Figures obtained from* [18].

Table 1.*) The mobility within the solvent saturated regions caused by the large adverse mobility ratio M and the lack of molecular diffusion should result in the front of the injected fluid progressing most rapidly along the diagonal between the injection and production wells. These effects are seen on the surface and contour plots in Figure* 2 *on the Cartesian mesh and imply that the flow is indeed strongest along the diagonal direction as expected. This effect is well studied in the literature and is referred to as the macroscopic fingering phenomenon* [25]*. Notably, our results at $t = 3$ with $k \geq 1$*

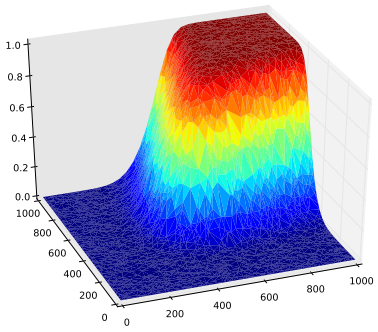

(a) Surface plot at $t = 3$ years.

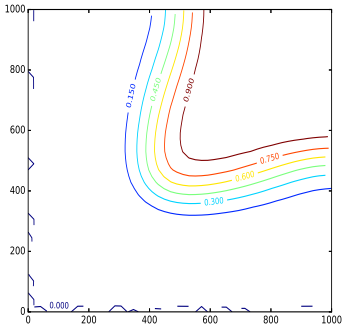

(b) Contour plot at $t = 3$ years

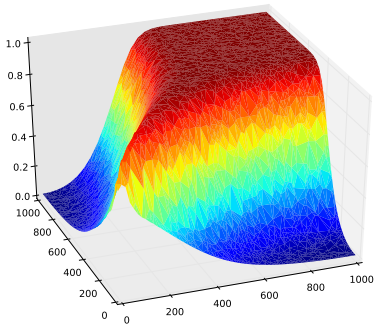

(c) Surface plot at $t = 10$ years.

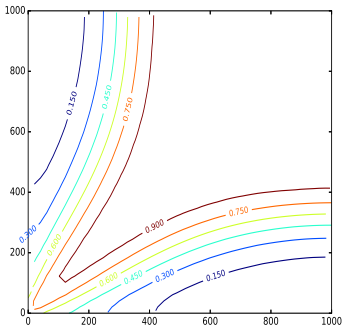

(d) Contour plot at $t = 10$ years.

FIG. 2. *Concentration of the invading solvent in Test* 4.1.1 *with* $k = 1$ *and* $\Delta t = 18$ *on Cartesian Mesh* 2 *with constant permeability.*

are far more realistic than those given in [7]*, which suffer from fluid progressing much too rapidly along the boundary of the domain. The scheme in* [7] *corresponds to a variant of the HHO method with* $k = 0$*; our own tests with* $k = 0$ *reproduced similar results as in this reference (see, e.g., Figures* 9(a) *and* 10(a)*).*

TEST 4.1.2. *We retain the parameters of Test* 4.1.1 *and use a hexagonal mesh in place of the Cartesian mesh (hexagonal Mesh* 4 *in Table* 1*). The fingering phenomenon is also observed in the results, which are shown in Figure* 3*, where we notice that there is a slight bias along the opposite diagonal at* $t = 3$*. This bias is expected, given that the mesh is skewed in this direction (see Figure* 1*), but it remains rather small and does not seem to impact much the final result at* $t = 10$ *years.*

TEST 4.1.3. *For this test, we take a discontinuous permeability tensor* $\boldsymbol{K} = 80\boldsymbol{I}$ *except on the four subdomains* $(200, 400)\times(200, 400)$*,* $(600, 800)\times(200, 400)$*,* $(200, 400)$ $\times$ $(600, 800)$*, and* $(600, 800)$ $\times$ $(600, 800)$*, where instead* $\boldsymbol{K} = 20\boldsymbol{I}$ *(see Figure* 4*). We use a* 40×40 *Cartesian for this test in order to ensure that the regions of discontinuity are aligned with the edges (Cartesian Mesh* 4 *in Table* 2*). The results shown in Figure* 5 *are of great interest to us as they depict very different behavior to those presented in* [7]*. Notably in* [7]*, by* $t = 10$ *years, the invading fluid has yet to subsume the two low permeability regions along the main diagonal. However, the HHO scheme depicts*

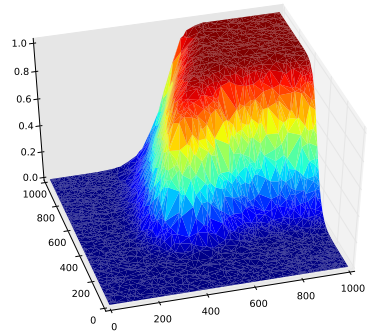

(a) Surface plot at $t = 3$ years.

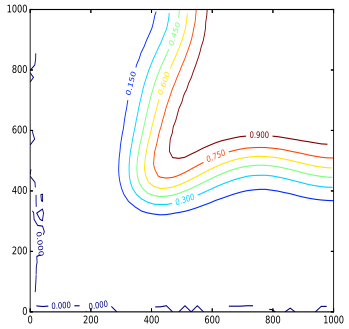

(b) Contour plot at $t = 3$ years.

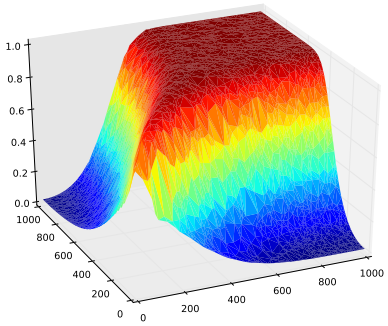

(c) Surface plot at $t = 10$ years.

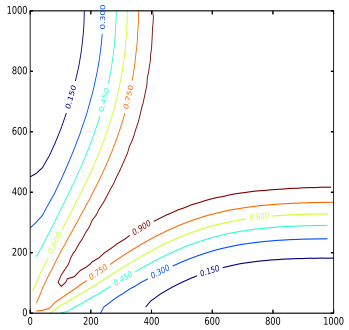

(d) Contour plot at $t = 10$ years.

FIG. 3. *Concentration of the invading solvent in Test* 4.1.1 *with* $k = 1$ *and* $\Delta t = 18$ *on Hexagonal Mesh* 2 *with constant permeability.*

both blocks almost entirely saturated by $t = 10$ *years. This implies the presence of a significantly higher amount of dispersion in the solution compared to that produced by the MFV scheme, which suggests that low-order schemes may underestimate the amount of diffusion described by the model. Finally, we note that the region saturated with solvent is larger when the permeability is inhomogeneous compared to Test* 4.1.1*, where it was not. This is another common phenomenon that has been well observed* [7, 40].

TEST 4.1.4. *We retain the parameters of Test* 4.1.3 *and use a triangular mesh in place of the Cartesian mesh. The mesh is a* 10×10 *grid of the triangular pattern depicted in Figure* 1 *(triangular Mesh* 2 *in Table* 2*), which ensures its alignment with the permeability discontinuities. The results can be seen in Figure* 6*, where we observe the same general distribution as in the Cartesian case, although the solvent seems slightly more dispersed. For such hybrid methods as the HHO method, it is well known that the main unknowns are the edge-based unknowns (see in particular section* 4.3*); it is therefore expected that, for a comparable mesh size, a mesh with fewer edges will perform slightly worse than a mesh with more edges. The Cartesian mesh used in Test* 4.1.3 *has* 1600 *cells,* 3280 *edges, and a size of* 6.25*; the triangular mesh used here has* 1400 *cells,* 2060 *edges, and a size of* 6.36.

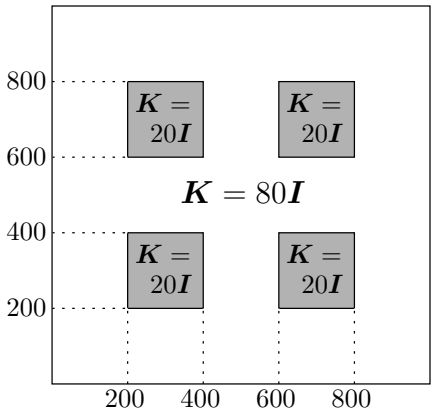

FIG. 4. *Permeability tensor for Tests* 4.1.3 *and* 4.1.4.

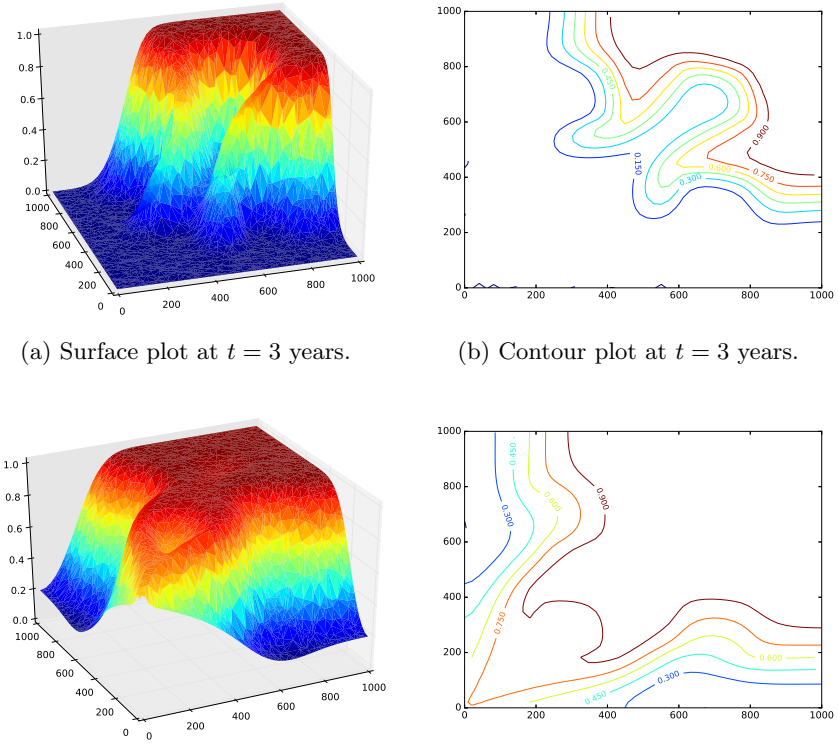

(a) Surface plot at $t = 3$ years.

(b) Contour plot at $t = 3$ years.

(c) Surface plot at $t = 10$ years.

(d) Contour plot at $t = 10$ years.

FIG. 5. *Concentration of the invading solvent in Test* 4.1.3 *with* $k = 1$ *and* $\Delta t = 18$ *on a* 40×40 *Cartesian mesh with a discontinuous permeability.*

4.2. Comparison of higher-order parameters. Although the scheme is arbitrary order in space and can easily be extended to arbitrary order in time (by substituting the Crank–Nicolson time-stepping for a higher-order scheme such as backward differentiation), we argue that the $k = 1$ scheme provides the best balance of accuracy

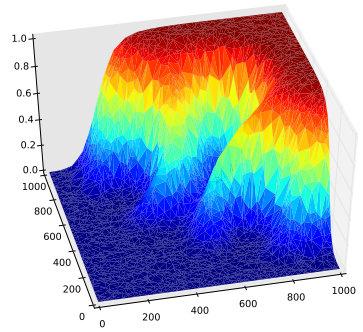

(a) Surface plot at $t = 3$ years.

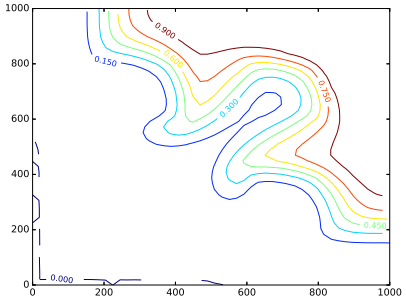

(b) Contour plot at $t = 3$ years.

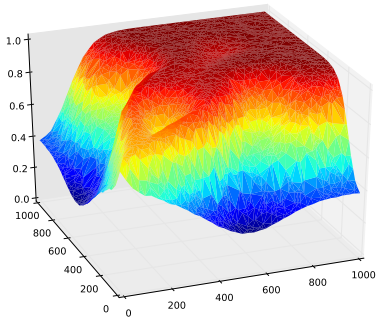

(c) Surface plot at $t = 10$ years.

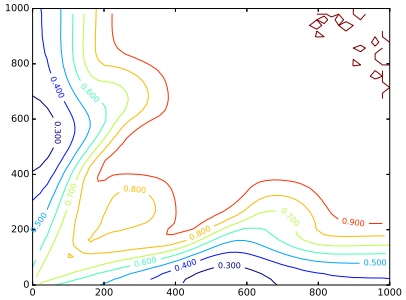

(d) Contour plot at $t = 10$ years.

FIG. 6. *Concentration of the invading solvent in Test* 4.1.3 *with* $k = 1$ *and* $\Delta t = 18$ *on a Triangular mesh with a discontinuous permeability.*

and computational efficiency. In order to demonstrate that this is the case, we present the following tests.

TEST 4.2.1. *To contrast the different solutions, we compare the principal quantity of interest to us, which is the total volume of oil recovered after ten years, as measured by the integral*

$$\int_\Omega \Phi(x) \mathrm{c}_h^N(x).$$

For the $k = 1$ *scheme as presented in Test* 4.1.1*, the total of volume of oil recovered can be measured to be* 65.798% *of the total volume of the reservoir. For the high-order tests, we range* k *from* 0 *to* 3*, and replace the Crank–Nicolson time-stepping scheme with a high-order backward differentiation formula of order* 4 *in order to minimize the contribution of the temporal error. Additionally, in order to mitigate the majority of the extrapolation error produced by the pressure estimate when extrapolating* c_h *(equation* (3.22)*), we take a reduced time-step of* $\Delta t = 7.2$ *days (approximately* $N = 500$ *steps.)*

Figure 7 *depicts the total recovery volume on each family of meshes in Table* 1 *with various polynomial degrees* k*. The* $k = 0$ *scheme is shown to perform quite poorly, producing results that are well out-of-line with the rest of the schemes. All of the other schemes however quickly converge to a similar estimate as the mesh size is refined,*

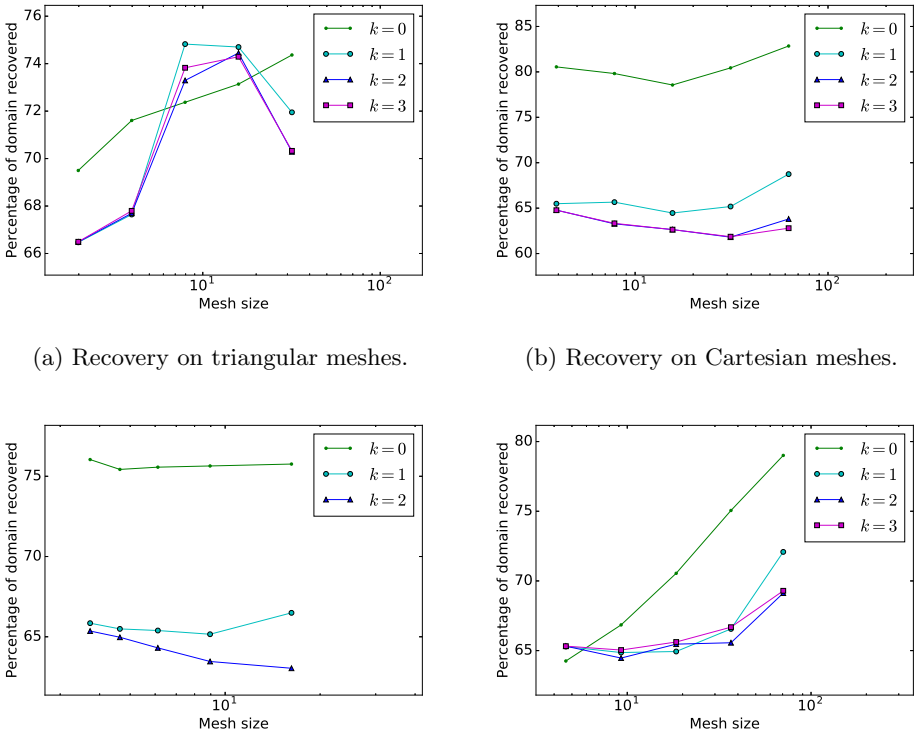

(a) Recovery on triangular meshes.

(b) Recovery on Cartesian meshes.

(c) Recovery on Kershaw meshes.

(d) Recovery on hexagonal meshes.

FIG. 7. *Total percentage of oil recovered from the reservoir with a uniform permeability, after* 10 *years and for various polynomial degrees and mesh sizes. To minimize the temporal error contribution, a high-order backward difference time-stepping scheme with* $\Delta t = 7.2$ *is used.*

which is consistently within 1% *of the estimate produced by Test* 4.1.1 *with only* $k = 1$*, a Crank–Nicolson time-stepping, and* $\Delta t = 18$ *days. We note that the scheme behaves well even on distorted meshes (the Kershaw mesh) until* $k = 3$*, where the linear system becomes too difficult to solve (Figure* 7 (c)*). This solvability issue of HHO with high degrees (remember that for* $k = 3$*, the pressure equation is approximated with an order* $2k = 6$*) on severely distorted meshes has already been noticed even for the Poisson problem and might be a consequence of rounding errors* [14]*. A way to mitigate this poor conditioning of the system matrix on skewed meshes is to change the local basis functions by applying a Gram–Schmidt orthonormalization process; see* [3]*. We however did not explore this option here as, in our experiments, the quality of the results do not significantly improve when using orders higher than* $k = 1$ *or* 2*, and the computational cost increases drastically.*

Finally, we also compare the high-order schemes on the discontinuous permeability tensor of Test 4.1.3*, using otherwise the same parameters. We use the mesh families, described in Table* 2*, whose edges are aligned with the discontinuities depicted in Figure* 4*. The results in Figure* 8 *show that we obtain similar convergence patterns to those of the homogeneous permeability tests. The* $k = 0$ *scheme still produces results that are well out of line with the rest, while all* $k \geq 1$ *schemes converge to a similar value as the mesh is refined.*

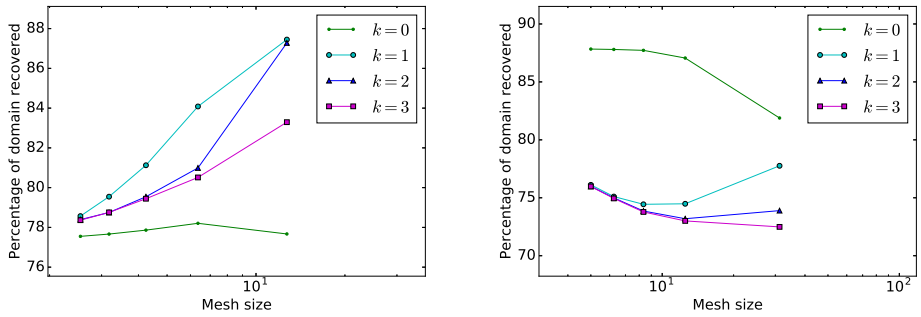

(a) Recovery on triangular meshes. (b) Recovery on Cartesian meshes.

FIG. 8. *Total percentage of oil recovered from the reservoir with a discontinuous permeability tensor, after* 10 *years for various polynomial degrees and mesh sizes. To minimize the temporal error contribution, a high-order backward difference time-stepping scheme with* $\Delta t = 7.2$ *is used.*

TEST 4.2.2. *The quality of the numerical approximations for various values of* k *can also be observed visually. Depicted in Figures* 9 *and* 10 *are the contour plots for the solution to Test* 4.1.1 *using* $k = 0, 1, 2, 3$ *at time* $t = 3$ *and* $t = 10$*, respectively. The low-order solution using* $k = 0$ *suffers from obvious grid effects in which the fluid mixture is progressing too rapidly along and clinging to the boundary of the domain. A similar effect is present in the results of the MFV scheme of* [7]*, suggesting that this artifact is a result of the low order of the scheme. Moving to a higher-order scheme, even just* $k = 1$*, remedies this effect and shows the solvent mixture progressing in a physically realistic pattern.*

The results of Figures 7, 8, 9, *and* 10 *also show that there is little advantage in selecting a spatial order* $k \geq 2$*, since the results for these higher orders are qualitatively and quantitatively similar to those obtained with* $k = 1$*.*

4.3. Computational cost. High-order versions of the HHO scheme have been shown to produce very reliable results. This increased accuracy however obviously comes with a higher computational cost than low-order schemes. The HHO method has been designed to allow for a static condensation of the cell unknowns: by local Gaussian elimination, the systems (3.21) and (3.35) can be expressed in terms of the face unknowns, resulting in systems on the face unknowns only and with the same sparsity structure as the original equations. On a given mesh $\mathcal{M}_h = (\mathcal{T}_h, \mathcal{F}_h)$ with polynomials of degree m, the global system is therefore of size

$$\binom{m+d-1}{d-1}|\mathcal{F}_h|,$$

and has an $\mathcal{O}(m^{d-1})$ growth with respect to the polynomial degree. Recall that the pressure is solved at a degree $m = 2k$. The cost of the time discretizations can be considered independent since it is clearly linear in the number of time-steps N.

Figure 11 illustrates the relative costs of the methods for various degrees k. Depicted are the average times taken per step using $N = 100$ time-steps for the data given in Test 4.1.1 on the mesh families in Table 1. We emphasize that our implementation is not optimized for high performance and that the tests are performed on a personal computer. These measurements are not intended to give an absolute estimate of the cost, only a comparison of running times of the various-order schemes. (This

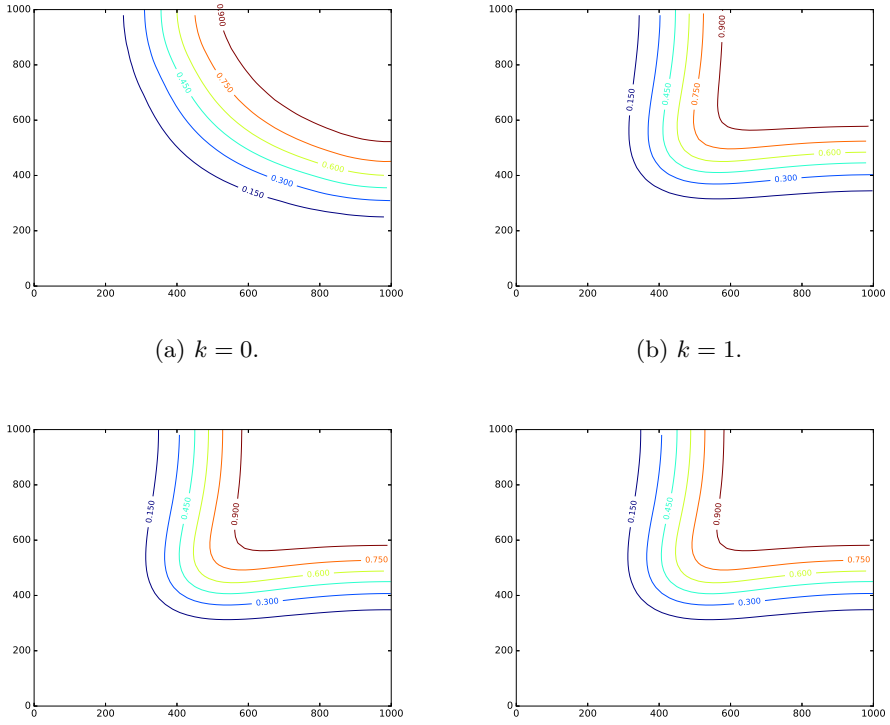

(a) $k = 0$. (b) $k = 1$.

(c) $k = 2$. (d) $k = 3$.

FIG. 9. *Comparison of the quality of the numerical approximation for $k = 0, 1, 2, 3$ on a Cartesian mesh at time $t = 3$ years. For $k = 0$, the fluid mixture clings to and overly rapidly progresses along the reservoir boundary. Moreover, the expected fingering effect is not visible. These issues are remedied by already selecting $k = 1$, and further increases of the order does not noticeably impact the solution (at least visually).*

comparison is valid since all tests were done on the same computer.) It is expected that, even if the times vary from one computer to the other, the relative positions of the curves corresponding to various k will be similar to those in Figure 11.

As predicted, the running times begin to grow very rapidly for fine meshes with high-order k. Since the number of degrees of freedom of the scheme is directly tied to the number of faces in the mesh, the execution time can be seen to be larger for meshes with a greater number of faces (see Table 1). Combined with the qualitative and quantitative results in sections 4.1 and 4.2, these relative running times further support our argument that the $k = 1$ scheme may be the best balance of accuracy and speed.

5. Conclusion. We designed and implemented an arbitrary-order scheme for a miscible incompressible flow model used in tertiary oil recovery. The scheme was based on the HHO method and is applicable on any kind of polygonal or polyhedral meshes. To ensure the stability of the numerical approximation, the pressure equation has to be approximated with an order twice as large as the order used for the concentration equation, and special care must be taken in reconstructing advective Darcy fluxes from the approximate pressure.

We produced several numerical tests on classical two-dimensional (2D) test cases encountered in the literature. These tests show that the best balance of accuracy

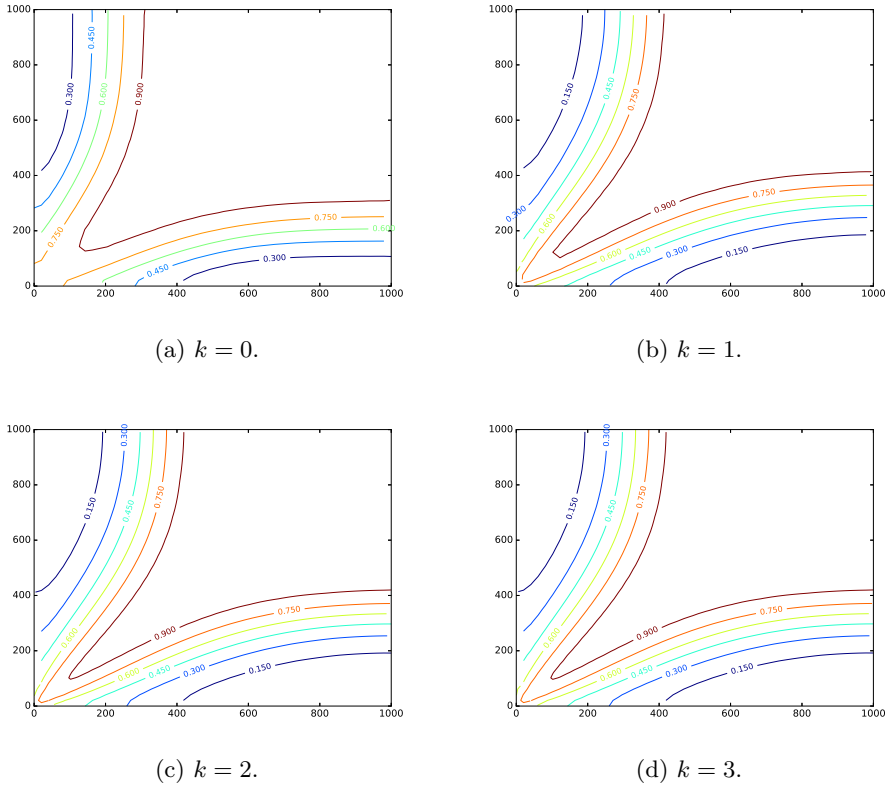

(a) $k = 0$. (b) $k = 1$.

(c) $k = 2$. (d) $k = 3$.

FIG. 10. *Comparison of the quality of the numerical approximation for $k = 0, 1, 2, 3$ on a Cartesian mesh at time $t = 10$ years.*

vs. computational cost is obtained by selecting a spatial order $k = 1$ and a Crank–Nicolson time-stepping. The results are stable with respect to the geometry of the meshes, in the sense that the total recovered oil is similar for all meshes and $k \geq 1$. Selecting an order $k = 1$ fixes grid effects that are present with $k = 0$ (as in low-order finite volume methods).

6. Appendix: Existence and stability of the solution to the scheme. Let $\mathcal{M}_h = (\mathcal{T}_h, \mathcal{F}_h)$ be a mesh. As in [16], we take a matching simplicial subdivision $\mathcal{I}_h$ of $\mathcal{M}_h$ and $\varrho > 0$ such that for any simplex $S \in \mathcal{I}_h$ of diameter h_S and inradius r_S, $\varrho h_S \leq r_S$, and for all $T \in \mathcal{T}_h$ and all $S \in \mathcal{I}_h$ such that $S \subset T$, $\varrho h_T \leq h_S$. In the following, $A \lesssim B$ means that $A \leq CB$ for some C depending only on Ω and ϱ (not on h).

The following lemma states a stability result for the discrete elliptic bilinear form. A proof can be found for $\Lambda = \mathrm{Id}$ in [18], and a sketch for extending this to generic Λ is given in [17].

LEMMA 6.1. *Let $\mathbf{\Lambda}$ be a bounded, symmetric, uniformly coercive tensor-valued function on Ω. Then for any $\underline{\mathrm{w}}_h \in X_h^k$, the discrete diffusive bilinear form $a_{h,\mathbf{\Lambda}}$ (3.19) satisfies*

$$a_{h,\mathbf{\Lambda}}(\underline{\mathrm{w}}_h, \underline{\mathrm{w}}_h) \gtrsim \sum_{T \in \mathcal{T}_h} \|\mathbf{\Lambda}^{\frac{1}{2}} \nabla \mathrm{w}_T\|^2_{L^2(T)} + \sum_{T \in \mathcal{T}_h} \sum_{F \in \mathcal{F}_T} \frac{\mathbf{\Lambda}_{TF}}{h_F} \|\mathrm{w}_F - \mathrm{w}_T\|^2_{L^2(F)}. \tag{6.1}$$

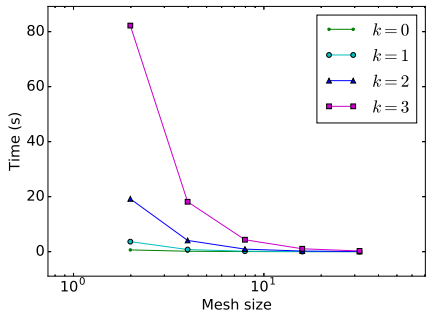

(a) Execution time on triangular meshes.

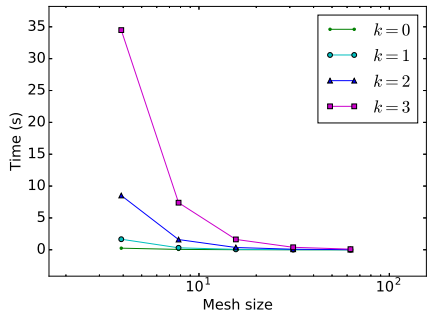

(b) Execution time on Cartesian meshes.

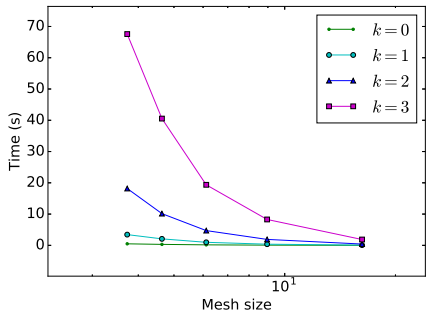

(c) Execution time on Kershaw meshes.

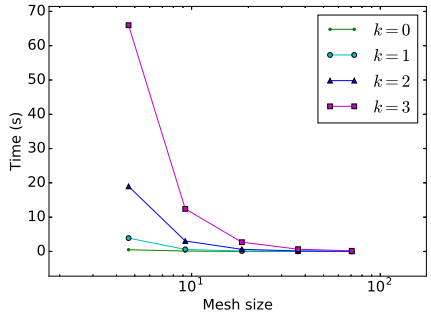

(d) Execution time on hexagonal meshes.

FIG. 11. *The average execution time for one time-step of Test* 4.1.1 *on various meshes.*

The following lemma is the key ingredient in proving the stability of the solution to the scheme. It holds true because of the specific choice of reconstructed Darcy velocity, chosen to be compatible with the discretization of the concentration equation.

LEMMA 6.2. *Let* R *be given by* (3.31) *and* $((\mathbf{U}_T)_{T\in\mathcal{T}_h}, (\mathrm{U}_{TF})_{T\in\mathcal{T}_h, F\in\mathcal{F}_T})$ *be the reconstructed Darcy velocity* (3.24)–(3.26) *corresponding to a solution* $\underline{\mathrm{p}}_h^{n+1/2}$ *of the discrete pressure equation* (3.21). *Then for any* $\underline{\mathrm{w}}_h \in X_h^k$, *the discrete advection-reaction bilinear form* (3.33) *satisfies*

$$a_{h,R,\mathbf{U}}(\underline{\mathrm{w}}_h, \underline{\mathrm{w}}_h) \geq \int_\Omega \frac{2\Phi}{\Delta t}\mathrm{w}_h^2 + \sum_{T\in\mathcal{T}_h}\sum_{F\in\mathcal{F}_T}\frac{1}{2}\int_F |\mathrm{U}_{TF}|(\mathrm{w}_T - \mathrm{w}_F)^2. \tag{6.2}$$

Proof. Equations (3.30) and (3.33) give

$$a_{h,R,\mathbf{U}}(\underline{\mathrm{w}}_h, \underline{\mathrm{w}}_h) = \sum_{T\in\mathcal{T}_h}\left\{-\int_T \mathrm{w}_T(\mathcal{G}_{T,\mathbf{U}}^k\underline{\mathrm{w}}_T) + \int_T R\mathrm{w}_T^2 + s^-_{\mathbf{U},T}(\underline{\mathrm{w}}_T, \underline{\mathrm{w}}_T)\right\}. \tag{6.3}$$

Expanding via the definitions of the advective derivative $\mathcal{G}_{T,\mathbf{U}}^k$ (Definition 3.6), the advection stabilization $s^-_{\mathbf{U},T}$ (3.32), and the reaction terms R (3.31) and collecting

cell and face terms, we find

$$
\begin{aligned}
a_{h,R,\mathbf{U}}(\underline{\mathrm{w}}_h, \underline{\mathrm{w}}_h) = &\sum_{T\in\mathcal{T}_h} \left\{ \int_T \frac{2\Phi}{\Delta t} \mathrm{w}_T^2 - \int_T (\mathbf{U}_T \cdot \nabla \mathrm{w}_T)\mathrm{w}_T + \int_T q^-(t^{n+1/2},\cdot)\mathrm{w}_T^2 \right\} \\
&+ \sum_{T\in\mathcal{T}_h} \sum_{F\in\mathcal{F}_T} \left\{ -\int_F \mathrm{U}_{TF}(\mathrm{w}_F - \mathrm{w}_T)\mathrm{w}_T + \int_F [\mathrm{U}_{TF}]^- (\mathrm{w}_F - \mathrm{w}_T)^2 \right\}.
\end{aligned} \tag{6.4}
$$

Considering the second cell term of (6.4), we notice that

$$
-(\mathbf{U}_T \cdot \nabla \mathrm{w}_T)\mathrm{w}_T = -\mathbf{U}_T \cdot \nabla \left(\frac{1}{2} \mathrm{w}_T^2 \right). \tag{6.5}
$$

Next we make use of the identity $(a-b)a = a^2 - ab = \frac{1}{2}(a^2-b^2) + \frac{1}{2}(a-b)^2$ to rewrite the first face term of (6.4) as

$$
-\int_F (\mathrm{U}_{TF}(\mathrm{w}_F - \mathrm{w}_T))\mathrm{w}_T = \frac{1}{2}\int_F \mathrm{U}_{TF}(\mathrm{w}_T^2 - \mathrm{w}_F^2) + \frac{1}{2}\int_F \mathrm{U}_{TF}(\mathrm{w}_T - \mathrm{w}_F)^2. \tag{6.6}
$$

Inspired by (6.5) and (6.6), we set for any cell $T \in \mathcal{T}_h$,

$$
\widetilde{\underline{\mathrm{w}}}_T = \frac{1}{2}\left(\mathrm{w}_T^2, \left(\mathrm{w}_F^2\right)_{F\in\mathcal{F}_T} \right) \in X_T^{2k}, \tag{6.7}
$$

and use the conservation of the fluxes (Theorem 3.5) with $\widetilde{\underline{\mathrm{w}}}_T$ instead of $\underline{\mathrm{w}}_T$ to write

$$
\begin{aligned}
&-\frac{1}{2}\int_T \mathbf{U}_T \cdot \nabla\left(\mathrm{w}_T^2\right) + \frac{1}{2}\sum_{F\in\mathcal{F}_T}\int_F \mathrm{U}_{TF}(\mathrm{w}_T^2 - \mathrm{w}_F^2) \\
&\quad = -\int_T \mathbf{U}_T \cdot \nabla \widetilde{\mathrm{w}}_T + \sum_{F\in\mathcal{F}_T}\int_F \mathrm{U}_{TF}(\widetilde{\mathrm{w}}_T - \widetilde{\mathrm{w}}_F) = a_{T,\boldsymbol{\kappa}^{n+1/2}}(\underline{\mathrm{p}}_T^{n+1/2}, \widetilde{\underline{\mathrm{w}}}_T).
\end{aligned} \tag{6.8}
$$

Summing over the cells and using the fact that $\underline{\mathrm{p}}_T^{n+1/2}$ solves the discrete pressure equation (3.21), we deduce that

$$
\begin{aligned}
&-\frac{1}{2}\sum_{T\in\mathcal{T}_h}\int_T \mathbf{U}_T \cdot \nabla\left(\mathrm{w}_T^2\right) + \frac{1}{2}\sum_{T\in\mathcal{T}_h}\sum_{F\in\mathcal{F}_T}\int_F \mathrm{U}_{TF}(\mathrm{w}_T^2 - \mathrm{w}_F^2) \\
&\quad = l_h^{p,n+1/2}(\widetilde{\underline{\mathrm{w}}}_h) = \sum_{T\in\mathcal{T}_h}\frac{1}{2}\int_T (q^+(t^{n+1/2},\cdot) - q^-(t^{n+1/2},\cdot))\mathrm{w}_T^2.
\end{aligned} \tag{6.9}
$$

Gathering the results from (6.6)–(6.9) and substituting into (6.4), we have

$$
\begin{aligned}
&a_{h,R,\mathbf{U}}(\underline{\mathrm{w}}_h, \underline{\mathrm{w}}_h) \\
&= \sum_{T\in\mathcal{T}_h} \left\{ \int_T \frac{2\Phi}{\Delta t}\mathrm{w}_T^2 + \frac{1}{2}\int_T (q^+(t^{n+1/2},\cdot) - q^-(t^{n+1/2},\cdot))\mathrm{w}_T^2 + \int_T q^-(t^{n+1/2},\cdot)\mathrm{w}_T^2 \right\} \\
&+ \sum_{T\in\mathcal{T}_h}\sum_{F\in\mathcal{F}_T} \left\{ \frac{1}{2}\int_F \mathrm{U}_{TF}(\mathrm{w}_T - \mathrm{w}_F)^2 + \int_F [\mathrm{U}_{TF}]^- (\mathrm{w}_F - \mathrm{w}_T)^2 \right\}.
\end{aligned} \tag{6.10}
$$

Combining the second and third cell terms of (6.10), and using $\frac{1}{2}\mathrm{U}_{TF} + [\mathrm{U}_{TF}]^- = \frac{1}{2}|\mathrm{U}_{TF}|$ and the nonnegativity of q^+ and q^-, we find

$$\begin{aligned} a_{h,R,\mathbf{U}}(\underline{\mathrm{w}}_h, \underline{\mathrm{w}}_h) = &\sum_{T\in\mathcal{T}_h}\left\{\int_T \frac{2\Phi}{\Delta t}\mathrm{w}_T^2 + \frac{1}{2}\int_T (q^+(t^{n+1/2},\cdot) + q^-(t^{n+1/2},\cdot))\mathrm{w}_T^2\right\} \\ &+ \sum_{T\in\mathcal{T}_h}\sum_{F\in\mathcal{F}_T}\frac{1}{2}\int_F |\mathrm{U}_{TF}|(\mathrm{w}_T - \mathrm{w}_F)^2 \\ \geq &\int_\Omega \frac{2\Phi}{\Delta t}\mathrm{w}_h^2 + \sum_{T\in\mathcal{T}_h}\sum_{F\in\mathcal{F}_T}\frac{1}{2}\int_F |\mathrm{U}_{TF}|(\mathrm{w}_T - \mathrm{w}_F)^2. \end{aligned}$$

The proof is complete. ∎

Remark 6.3 (order $2k$ on the pressure, and choice of the Darcy fluxes). The reason for discretizing the pressure equation with an HHO scheme of order $2k$, instead of k, is found in (6.8). Obtaining this relation requires the usage of $\widetilde{\underline{\mathrm{w}}}_T$, defined by (6.7) and belonging to X_T^{2k}, into (3.27).

Equation (6.8) is an essential component of the stability proof, and it also justifies our choice of Darcy flux and volumetric velocity (3.24) and (3.26).

We are now ready to prove the existence, uniqueness, and stability of the solution to the scheme.

Proof of Theorem 3.7. Let us first assume that we have a solution $(\underline{\mathrm{p}}_h, \underline{\mathrm{c}}_h)$ to the scheme, and let us prove the a priori estimate (3.36). By (3.35), we have for all $\underline{\mathrm{w}}_h \in X_h^k$

$$a_{h,\mathbf{D},R,\mathbf{U}}(\underline{\mathrm{c}}_h^{n+1/2}, \underline{\mathrm{w}}_h) = l_h^{c,n+1/2}(\underline{\mathrm{w}}_h). \tag{6.11}$$

Select $\underline{\mathrm{w}}_h = \underline{\mathrm{c}}_h^{n+1/2}$ as the test function and expand by the definitions of the discrete linear forms to write

$$a_{h,\mathbf{D}}(\underline{\mathrm{c}}_h^{n+1/2}, \underline{\mathrm{c}}_h^{n+1/2}) + a_{h,R,\mathbf{U}}(\underline{\mathrm{c}}_h^{n+1/2}, \underline{\mathrm{c}}_h^{n+1/2}) = l_h^{c,n+1/2}(\underline{\mathrm{c}}_h^{n+1/2}).$$

Using Lemma 6.1 (with $\mathbf{\Lambda} = \mathbf{D}$) and Lemma 6.2, the definition (3.34) of $l^{c,n+1/2}$ then yields

$$\begin{aligned} &\int_\Omega \frac{2\Phi(\mathrm{c}_h^{n+1/2})^2}{\Delta t} + \sum_{T\in\mathcal{T}_h}\sum_{F\in\mathcal{F}_h}\frac{\beta}{h_F}\|\mathrm{c}_F^{n+1/2} - \mathrm{c}_T^{n+1/2}\|_{L^2(F)}^2 \\ &\qquad \leq \int_\Omega \left(q^+(t^{n+1/2},\cdot)\hat{c}(t^{n+1/2},\cdot) + \frac{2\Phi}{\Delta t}\mathrm{c}_h^n\right)\mathrm{c}_h^{n+1/2}, \end{aligned} \tag{6.12}$$

where $\beta > 0$ is a coercivity constant of $\mathbf{D}$ (β depends on Φ, d_m, d_l, and d_t). Gathering the time-stepping terms together and dropping the second term in the left-hand side, we then write

$$\int_\Omega \frac{2\Phi(\mathrm{c}_h^{n+1/2} - \mathrm{c}_h^n)}{\Delta t}\mathrm{c}_h^{n+1/2} \leq \int_\Omega \left(q^+(t^{n+1/2},\cdot)\hat{c}(t^{n+1/2},\cdot)\right)\mathrm{c}_h^{n+1/2}. \tag{6.13}$$

Recalling the definition of the half time-stepped concentration (3.3), we easily deduce

$$\int_\Omega \frac{2\Phi(\mathrm{c}_h^{n+1/2} - \mathrm{c}_h^n)}{\Delta t}\mathrm{c}_h^{n+1/2} = \int_\Omega \Phi\frac{(\mathrm{c}_h^{n+1})^2 - (\mathrm{c}_h^n)^2}{2\Delta t}.$$

Hence, using the Cauchy–Schwarz and Young inequalities in the right-hand side of (6.13) yields, for any $\varepsilon > 0$,

$$\begin{aligned}\int_\Omega \Phi \frac{(\mathrm{c}_h^{n+1})^2 - (\mathrm{c}_h^n)^2}{2\Delta t} &\le \|q^+(t^{n+1/2},\cdot)\hat{c}(t^{n+1/2},\cdot)\|_{L^2(\Omega)} \|\mathrm{c}_h^{n+1/2}\|_{L^2(\Omega)} \\ &\le \frac{1}{2\varepsilon}\|q^+(t^{n+1/2},\cdot)\hat{c}(t^{n+1/2},\cdot)\|_{L^2(\Omega)}^2 + \frac{\varepsilon}{2}\|\mathrm{c}_h^{n+1/2}\|_{L^2(\Omega)}^2.\end{aligned}$$

Summing over the time-steps $n = 0, \dots, N-1$, the sum telescopes in the left-hand side. Using $|\widehat{c}| \le 1$ and, by convexity of the square function,

$$(\mathrm{c}_h^{n+1/2})^2 = \left(\frac{\mathrm{c}_h^n + \mathrm{c}_h^{n+1}}{2}\right)^2 \le \frac{(\mathrm{c}_h^n)^2 + (\mathrm{c}_h^{n+1})^2}{2}$$

we infer

$$\begin{aligned}\int_\Omega \Phi \frac{(\mathrm{c}_h^N)^2 - (\mathrm{c}_h^0)^2}{2\Delta t} &\le \frac{N}{2\varepsilon}\|q^+\|_{L^\infty(0,t_f;L^2(\Omega))}^2 \\ &\quad + \frac{\varepsilon}{4}\sum_{n=0}^{N-1}\left(\|\mathrm{c}_h^n\|_{L^2(\Omega)}^2 + \|\mathrm{c}_h^{n+1}\|_{L^2(\Omega)}^2\right) \\ &\le \frac{N}{2\varepsilon}\|q^+\|_{L^\infty(0,t_f;L^2(\Omega))}^2 + \frac{\varepsilon}{2}\sum_{n=0}^{N}\|\mathrm{c}_h^n\|_{L^2(\Omega)}^2.\end{aligned}$$

Applying the boundedness of Φ (2.2a),

$$\int_\Omega \Phi_* \frac{(\mathrm{c}_h^N)^2}{2\Delta t} \le \int_\Omega \Phi_*^{-1}\frac{(\mathrm{c}_h^0)^2}{2\Delta t} + \frac{N}{2\varepsilon}\|q^+\|_{L^\infty(0,t_f;L^2(\Omega))}^2 + \frac{\varepsilon}{2}\sum_{n=0}^{N}\int_\Omega (\mathrm{c}_h^n)^2.$$

Multiplying both sides by $2\Delta t/\Phi_*$ and recalling that $N\Delta t = t_f$ yields

$$\int_\Omega (\mathrm{c}_h^N)^2 \le \int_\Omega \frac{(\mathrm{c}_h^0)^2}{\Phi_*^2} + \frac{t_f}{\varepsilon\Phi_*}\|q^+\|_{L^\infty(0,t_f;L^2(\Omega))}^2 + \frac{\varepsilon t_f}{\Phi_* N}\sum_{n=0}^{N}\int_\Omega (\mathrm{c}_h^n)^2. \tag{6.14}$$

Take $\varepsilon = \frac{\Phi_*}{2t_f}$, so that $\frac{\varepsilon t_f}{\Phi_* N} = \frac{1}{2N} < 1$. Applying the Gronwall inequality of [31, Lemma 5.1] yields

$$\|\mathrm{c}_h^N\|_{L^2(\Omega)}^2 \le \exp\left(\frac{1}{2N}\sum_{n=0}^{N}\frac{2N}{2N-1}\right)\left(\frac{\|\mathrm{c}_h^0\|_{L^2(\Omega)}^2}{\Phi_*^2} + \frac{t_f}{\varepsilon\Phi_*}\|q^+\|_{L^\infty(0,t_f;L^2(\Omega))}^2\right).$$

The proof of (3.36) is complete since $\frac{t_f}{\varepsilon\Phi_*} = \frac{2t_f^2}{\Phi_*^2}$ and $\frac{1}{2N}\sum_{n=0}^{N}\frac{2N}{2N-1} = \frac{N+1}{2N-1} \le 2$. The estimate was obtained for c_h^N but the same reasoning shows that it holds for c_h^n for all $n = 0, \dots, N$.

The existence and uniqueness of $(\underline{\mathrm{p}}_h, \underline{\mathrm{c}}_h)$ follows easily. At each iteration of Algorithm 1, $\underline{\mathrm{p}}_h^{n+1/2}$ is sought as a solution of the linear system (3.21)–(3.23). If $l_h^{p,n+1/2} = 0$, plugging $\underline{\mathrm{w}}_h = \underline{\mathrm{p}}_h^{n+1/2}$ in (3.21) and using Lemma 6.1 shows that the only possible solution to this linear system is zero. (By (6.1), all cell unknowns must be constant and, working from neighbor to neighbor, equal to all face unknowns and to all other

cell unknowns; then (3.23) fixes this constant uniform value to zero.) Hence, the matrix corresponding to (3.21)–(3.23) is invertible, which means that this system has a unique solution $\underline{\mathrm{p}}_h^{n+1/2}$ at each time-step. After the pressure is fixed, $\underline{\mathrm{c}}_h^{n+1/2}$ is sought as a solution to the linear equation (3.35). If $l_h^{c,n+1/2} = 0$, the right-hand side of (6.12) vanishes, which shows that all cell and face degrees of freedom are equal to 0. Hence, the matrix of (3.35) has a trivial kernel, which shows the existence and uniqueness of $\underline{\mathrm{c}}_h^{n+1/2}$ solution to this equation. ∎

7. Appendix: Implementation of the scheme. We present here algorithms for computing the local operators that define the numerical scheme. A fully functional implementation of the scheme in `C++` along with all of the tests present in section 4 can be found at https://github.com/DanielLiamAnderson/hho-peaceman.

The code for handling the mesh is a preliminary version of what later became the `DiSk++` library by Cicuttin, Pietro, and Ern [11].

7.1. A basis for the function spaces. In order to realize the algorithms for solving the pressure and concentration equations, we first need to express our function spaces and test functions concretely. We recall the space $\mathbb{P}^m(K)$ of polynomials of degree $\leq m$ over the domain K and decompose its elements in terms of the following basis functions. Denote by $(\bar{x}_K, \bar{y}_K)$ the center of mass of K, and by h_K its diameter. The basis functions for 2D elements $T \in \mathcal{T}_h$ are given by

$$\varphi_{r,s}^T : T \to \mathbb{R}, \qquad \varphi_{r,s}^T(x,y) = \left(\frac{x - \bar{x}_T}{h_T}\right)^r \left(\frac{y - \bar{y}_T}{h_T}\right)^s \tag{7.1}$$

for $r, s \geq 0$ and $r + s \leq m$. The basis functions for 1D elements $F \in \mathcal{F}_h$ are given by

$$\varphi_r^F : F \to \mathbb{R}, \qquad \varphi_r^F(x,y) = \left(\frac{(x - \bar{x}_F)(x_0 - \bar{x}_F)}{h_F^2} + \frac{(y - \bar{y}_F)(y_0 - \bar{y}_F)}{h_F^2}\right)^r \tag{7.2}$$

for $0 \leq r \leq m$, where (x_0, y_0) is one of the endpoints of F. We then take, for each cell $T \in \mathcal{T}_h$ and face $F \in \mathcal{F}_h$, the set of all basis functions covering the entire mesh, where each function is extended to Ω by defining $\varphi = 0$ outside its initial domain:

$$\mathcal{B}^m = \left(\bigcup_{T \in \mathcal{T}_h} \{\varphi_{r,s}^T\}_{r+s \leq m}\right) \bigcup \left(\bigcup_{F \in \mathcal{F}_h} \{\varphi_r^F\}_{r \leq m}\right). \tag{7.3}$$

The algorithms for solving the pressure and concentration equations then become square linear systems by evaluating the discrete equations (3.21) and (3.35) at all basis functions $\underline{\mathrm{w}}_h \in \mathcal{B}^m$. Since each basis function is only nonzero in a single element of the meshed domain, the resulting linear systems will be sparse. The following notation is referred to throughout the implementation.

- $\mathcal{B}^m$ the set of all basis functions over mesh elements up to degree m,
- $\mathcal{B}_K^m$ the basis functions on the cell or face K of degree up to m,
- $\mathcal{B}_K^{m,1}$ the basis functions on the cell or face K of degree at least 1, up to m,
- $\mathcal{B}_{\underline{T}}^m$ the basis functions on the cell T and all adjacent faces of degree up to m.

Remark 7.1. The space $\mathcal{B}_K^{m,1}$ is useful when considering gradients of high-order basis functions, since gradients of degree zero basis functions are identically zero.

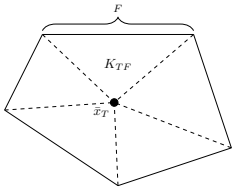

FIG. 12. *A cell split into triangular subelements to facilitate numerical quadrature.*

7.2. Numerical quadrature. The assembly of the scheme matrices requires the numerical integration of products of arbitrary-order polynomial basis functions. To ensure no loss of accuracy or stability, sufficiently accurate numerical quadrature rules must be used. Most of the integrals that we are required to evaluate consist of the product of two or three degree m polynomials. Based on this observation, for polynomial degrees of freedom of order m, we employ numerical quadrature schemes that are exact for polynomials of degree up to $3m$. To integrate cell polynomials, we use the numerical quadrature schemes introduced by Dunavant in [24]. The Dunavant quadrature rules provide exact integrals for fixed degree polynomial functions on triangular domains so we will split each cell of the mesh into triangular subelements such that each face of the cell corresponds to one subelement. Quadrature for edge polynomials is performed using standard Gaussian quadrature rules for one dimensional domains.

In the algorithms that follow, K_{TF} stands for the triangular subelement of the cell T adjacent to the edge $F \in \mathcal{F}_T$ as depicted in Figure 12.

7.3. Assembly of the local operators for the pressure scheme. The majority of the integrals in (3.21) will be zero, so the local operators $a_{T,\mathbf{\Lambda}}$ can be efficiently assembled for each cell and then combined to form a sparse matrix for the scheme. These local constructions are outlined in the following algorithms. Algorithm 2 demonstrates the computation of local gradient reconstruction operator $\nabla \boldsymbol{r}_{T,\mathbf{\Lambda}}^{m+1}$ by inverting a high-order mass matrix of the basis gradient functions. The local gradient reconstruction is used in the assembly of the local diffusion operator $a_{T,\mathbf{\Lambda}}$ and in the reconstruction of the fluxes from the solution to the pressure equation. Algorithm 3 outlines the assembly of the local diffusion operator. The key step is the computation of the projections from the high-order correction, which is accomplished by computing a mass matrix of mixed high and low-order basis functions. Finally, Algorithm 4 presents the implementation of the pressure source term, i.e., the right-hand side of the equation.

7.4. Computation of the numerical fluxes. We now present a simple algorithm to compute the numerical fluxes U_{TF} that does not require us to compute the whole right-hand side of (3.24). Let $T \in \mathcal{T}_h$ and use the conservativity of the fluxes (Theorem 3.5) with a cell-absent test function $\underline{\mathrm{w}}_T = (0, \underline{\mathrm{w}}_F) \in \{0\} \times X_{\partial T}^{2k}$ to obtain

$$a_{T,\boldsymbol{\kappa}}(\underline{\mathrm{p}}_T, \underline{\mathrm{w}}_T) = -\sum_{F \in \mathcal{F}_T} (\mathrm{U}_{TF}, \mathrm{w}_F)_{L^2(F)}. \tag{7.4}$$

Select an edge $F \in \mathcal{F}_T$, then write the flux U_{TF} in terms of the basis $\mathcal{B}_F^{2k}$ like so

$$\mathrm{U}_{TF} = \sum_{i=0}^{|\mathcal{B}_F^{2k}|-1} \lambda_i^F \varphi_i^F. \tag{7.5}$$

Algorithm 2 Computation of the local gradient reconstruction matrix.

Set $M_{\varphi_i,\varphi_j} = 0$ for all $\varphi_i, \varphi_j \in \mathcal{B}_T^{m+1,1}$
Set $B_{\varphi_i,\varphi_j} = 0$ for all $\varphi_i \in \mathcal{B}_T^{m+1,1}, \varphi_j \in \mathcal{B}_{\underline{T}}^m$
for each edge $F \in F_T$ **do**
  ▷ Compute volumetric terms corresponding to the subelement of F
  for each quadrature node (x, w_x) of K_{TF} **do**
    for each basis function $\varphi_i \in \mathcal{B}_T^{m+1,1}$ **do**
      for each basis function $\varphi_j \in \mathcal{B}_T^{m+1,1}$ **do**
        $M_{\varphi_i,\varphi_j} \leftarrow M_{\varphi_i,\varphi_j} + w_x(\mathbf{\Lambda}(x)\nabla\varphi_i(x)) \cdot \nabla\varphi_j(x)$
      end for
      for each basis function $\varphi_j \in \mathcal{B}_T^m$ **do**
        $B_{\varphi_i,\varphi_j} \leftarrow B_{\varphi_i,\varphi_j} + w_x(\mathbf{\Lambda}(x)\nabla\varphi_i(x)) \cdot \nabla\varphi_j(x)$
      end for
    end for
  end for
  ▷ Compute edge terms
  for each quadrature node (x, w_x) of F **do**
    for each basis function $\varphi_i \in \mathcal{B}_T^{m+1,1}$ **do**
      for each basis function $\varphi_j \in \mathcal{B}_F^m$ **do**
        $B_{\varphi_i,\varphi_j} \leftarrow B_{\varphi_i,\varphi_j} + w_x\nabla\varphi_i(x) \cdot (\mathbf{\Lambda}(x)\mathbf{n}_{TF})\varphi_j(x)$
      end for
      for each basis function $\varphi_j \in \mathcal{B}_T^m$ **do**
        $B_{\varphi_i,\varphi_j} \leftarrow B_{\varphi_i,\varphi_j} - w_x\nabla\varphi_i(x) \cdot (\mathbf{\Lambda}(x)\mathbf{n}_{TF})\varphi_j(x)$
      end for
    end for
  end for
end for
Set $G = M^{-1}B$ ▷ Solve for the gradient reconstruction

The balance equation (7.4) now reads

$$a_{T,\boldsymbol{\kappa}}(\underline{\mathrm{p}}_T, \underline{\mathrm{w}}_T) = -\sum_{i=0}^{|\mathcal{B}_F^{2k}|-1} \lambda_i^F(\varphi_i^F, \mathrm{w}_F)_{L^2(F)}, \tag{7.6}$$

which results in a square linear system for $\{\lambda_i^F\}_i$ in terms of the basis functions $\mathcal{B}_F^{2k}$. The construction of the numerical fluxes is shown in Algorithm 5.

7.5. Assembly of the local operators for the concentration scheme. The computation of the advective derivative is similar to that of the local gradient reconstruction. Algorithm 6 shows how to efficiently compute $\mathcal{G}_{T,\mathbf{U}}^k$ for each cell $T \in \mathcal{T}_h$ by solving a local problem involving the mass matrix of the cell. The local advection-reaction operator is computed as shown in Algorithm 7 by assembling together the advective derivatives of the local test functions combined with a mass-reaction matrix that accounts for the value of the reaction terms. Last, we present Algorithm 8, which computes the right-hand side of the concentration equation.

Algorithm 3 Assembly of the local diffusion matrix.

▷ Compute mass matrices
Set $M^{TT}_{\varphi_i,\varphi_j} = 0$ for all $\varphi_i, \varphi_j \in \mathcal{B}^{m+1}_T$
Set $M^{TF}_{\varphi_i,\varphi_j} = 0$ for all $\varphi_i \in \mathcal{B}^m_F,\ \varphi_j \in \mathcal{B}^{m+1}_T$ for all edges $F \in \mathcal{F}_T$
Set $M^{FF}_{\varphi_i,\varphi_j} = 0$ for all $\varphi_i, \varphi_j \in \mathcal{B}^m_F$ for all edges $F \in \mathcal{F}_T$
for each edge $F \in F_T$ **do**
    ▷ Compute cell-on-cell mass matrix
    for each quadrature node (x, w_x) of K_{TF} **do**
        for each basis function $\varphi_i \in \mathcal{B}^{m+1}_T$ **do**
            for each basis function $\varphi_j \in \mathcal{B}^{m+1}_T$ **do**
                $M^{TT}_{\varphi_i,\varphi_j} \leftarrow M^{TT}_{\varphi_i,\varphi_j} + w_x \varphi_i(x)\varphi_j(x)$
            end for
        end for
    end for
    ▷ Compute cell-on-edge and edge-on-edge mass matrices
    for each quadrature node (x, w_x) of F **do**
        for each basis function $\varphi_i \in \mathcal{B}^m_F$ **do**
            for each basis function $\varphi_j \in \mathcal{B}^{m+1}_T$ **do**
                $M^{TF}_{\varphi_i,\varphi_j} \leftarrow M^{TF}_{\varphi_i,\varphi_j} + w_x \varphi_i(x)\varphi_j(x)$
            end for
        end for
        for each basis function $\varphi_i \in \mathcal{B}^m_F$ **do**
            for each basis function $\varphi_j \in \mathcal{B}^m_F$ **do**
                $M^{FF}_{\varphi_i,\varphi_j} \leftarrow M^{FF}_{\varphi_i,\varphi_j} + w_x \varphi_i(x)\varphi_j(x)$
            end for
        end for
    end for
end for
▷ Compute the volumetric term
Compute the gradient reconstruction G (Algorithm 2)
Set $A = B^{tr}G$ ▷ B^{tr} is the transpose of B from Algorithm 2
▷ Compute the local reconstruction cell projection matrix
Set $M^{TT,m}_{\varphi_i,\varphi_j} = M^{TT}_{\varphi_i,\varphi_j}$ for all $\varphi_i, \varphi_j \in \mathcal{B}^m_T$
Set $M^{TT,m+1}_{\varphi_i,\varphi_j} = M^{TT}_{\varphi_i,\varphi_j}$ for all $\varphi_i \in \mathcal{B}^m_T, \varphi_j \in \mathcal{B}^{m+1,1}_T$
Solve $M^{TT,m}P_T = M^{TT,m+1}$ for P_T
▷ Compute the edge terms
for each edge $F \in F_T$ **do**
    ▷ Compute the edge projection matrix
    Set $P_F = (M^{FF})^{-1}$
    Set $M^{TF,m}_{\varphi_i,\varphi_j} = M^{TF}_{\varphi_i,\varphi_j}$ for all $\varphi_i \in \mathcal{B}^m_F, \varphi_j \in \mathcal{B}^m_T$
    Set $M^{TF,m+1}_{\varphi_i,\varphi_j} = M^{TF}_{\varphi_i,\varphi_j}$ for all $\varphi_i \in \mathcal{B}^m_F, \varphi_j \in \mathcal{B}^{m+1,1}_T$
    ▷ Compute projections
    Set $B_F = P_F M^{TF,m+1}G - I_F$ ▷ I_F = identity matrix on the edge terms
    Set $B_T = P_F M^{TF,m}(I_T - P_T)$ ▷ I_T = identity matrix on the cell terms
    Set $B_{RF} = B_F + B_T$
    ▷ Compute local stabilization terms
    $A \leftarrow A + \frac{\mathbf{\Lambda}_{TF}}{h_F} B^{tr}_{RF} M^{FF} B_{RF}$
end for

Algorithm 4 Assembly of the pressure source vector.

Set $b_{\varphi_i} = 0$ for all $\varphi_i \in \mathcal{B}_{\underline{T}}^{2k}$
for each edge $F \in F_T$ **do**
  for each quadrature node (x, w_x) of K_{TF} **do**
    for each basis function $\varphi_i \in \mathcal{B}_T^{2k}$ **do**
      $b_{\varphi_i} \leftarrow b_{\varphi_i} + w_x \varphi_i(x)(q^+(t^{n+1/2}, x) - q^-(t^{n+1/2}, x))$
    end for
  end for
end for

Algorithm 5 Computation of the local fluxes.

Compute the local diffusion operator matrix A with $m = 2k$ (Algorithm 3)
for each edge $F \in \mathcal{F}_T$ **do**
  Set $\alpha_{\varphi_i} = 0$ for all $\varphi_i \in \mathcal{B}_F^{2k}$
  for each basis function $\varphi_i \in \mathcal{B}_F^{2k}$ **do**
    $\alpha_{\varphi_i} \leftarrow -(\underline{\mathrm{p}}_T \cdot A_{:,\varphi_i})$ ▷ $A_{:,\varphi_i}$ is the column of A corresponding to φ_i
  end for
  ▷ Build the Gram matrix
  Set $G_{\varphi_i,\varphi_j} = 0$ for all $\varphi_i, \varphi_j \in \mathcal{B}_F^{2k}$
  for each quadrature node (x, w_x) on F **do**
    for each basis function $\varphi_i \in \mathcal{B}_F^{2k}$ **do**
      for each basis function $\varphi_j \in \mathcal{B}_F^{2k}$ **do**
        $G_{\varphi_i,\varphi_j} \leftarrow G_{\varphi_i,\varphi_j} + w_x \varphi_i(x)\varphi_j(x)$
      end for
    end for
  end for
  Set $\lambda^F = G^{-1}\alpha$
end for
Compute U_{TF} in terms of λ^F as in (7.5)

Algorithm 6 Assembly of the local advective-reactive derivative matrix.

Set $M_{\varphi_i,\varphi_j} = 0$ for all $\varphi_i, \varphi_j \in \mathcal{B}_T^k$
Set $B_{\varphi_i,\varphi_j} = 0$ for all $\varphi_i \in \mathcal{B}_T^k, \varphi_j \in \mathcal{B}_{\underline{T}}^k$
for each edge $F \in \mathcal{F}_T$ **do**
    ▷ Compute the volumetric terms
    for each quadrature node (x, w_x) in K_{TF} **do**
        for each basis function $\varphi_i \in \mathcal{B}_T^k$ **do**
            for each basis function $\varphi_j \in \mathcal{B}_T^k$ **do**
                $M_{\varphi_i,\varphi_j} \leftarrow M_{\varphi_i,\varphi_j} + w_x \varphi_i(x)\varphi_j(x)$
                $B_{\varphi_i,\varphi_j} \leftarrow B_{\varphi_i,\varphi_j} + w_x(\mathrm{U}_{TF}(x) \cdot \nabla\varphi_i(x))\varphi_j(x)$
            end for
        end for
    end for
    ▷ Compute the edge terms
    for each quadrature node (x, w_x) on F **do**
        for each basis function $\varphi_i \in \mathcal{B}_T^k$ **do**
            for each basis function $\varphi_j \in \mathcal{B}_F^k$ **do**
                $B_{\varphi_i,\varphi_j} \leftarrow B_{\varphi_i,\varphi_j} + w_x(\mathrm{U}_{TF}(x) \cdot \mathbf{n}_{TF})\varphi_i(x)\varphi_j(x)$
            end for
            for each basis function $\varphi_j \in \mathcal{B}_T^k$ **do**
                $B_{\varphi_i,\varphi_j} \leftarrow B_{\varphi_i,\varphi_j} - w_x(\mathrm{U}_{TF}(x) \cdot \mathbf{n}_{TF})\varphi_i(x)\varphi_j(x)$
            end for
        end for
    end for
end for
▷ Solve for the advective-reaction derivative
Set $G = M^{-1}B$

Algorithm 7 Assembly of the local advection-reaction matrix.

Set $A_{\varphi_i,\varphi_j} = 0$ for all $\varphi_i, \varphi_j \in \mathcal{B}_{\underline{T}}^k$
Compute the advective-reactive derivative G (Algorithm 6)
for each edge $F \in \mathcal{F}_T$ **do**
  ▷ Compute the volumetric terms
  for each quadrature node (x, w_x) in K_{TF} **do**
    for each basis function $\varphi_i \in \mathcal{B}_T^k$ **do**
      for each basis function $\varphi_j \in \mathcal{B}_T^k$ **do**
        $A_{\varphi_i,\varphi_j} \leftarrow A_{\varphi_i,\varphi_j} + w_x \varphi_i(x)\varphi_j(x)\mu(x)$
      end for
    end for
    for each basis function $\varphi_i \in \mathcal{B}_{\underline{T}}^k$ **do**
      ▷ Compute $\mathcal{G}_{T,\mathbf{U}}^k \underline{\mathrm{W}}_{\underline{T}}$
      Set $v = 0$
      for each basis function $\varphi_j \in \mathcal{B}_T^k$ **do**
        $v \leftarrow v + \varphi_j(x) G_{\varphi_j,\varphi_i}$
      end for
      for each basis function $\varphi_j \in \mathcal{B}_T^k$ **do**
        $A_{\varphi_i,\varphi_j} \leftarrow A_{\varphi_i,\varphi_j} - w_x \varphi_j(x) v$
      end for
    end for
  end for
  ▷ Compute the edge terms
  for each quadrature node (x, w_x) on F **do**
    for each basis function $\varphi_i \in \mathcal{B}_T^k$ **do**
      for each basis function $\varphi_j \in \mathcal{B}_F^k$ **do**
        $A_{\varphi_i,\varphi_j} \leftarrow A_{\varphi_i,\varphi_j} - w_x [\mathrm{U}_{TF}(x) \cdot \mathbf{n}_{TF}]^- \varphi_i(x)\varphi_j(x)$
        $A_{\varphi_j,\varphi_i} \leftarrow A_{\varphi_j,\varphi_i} - w_x [\mathrm{U}_{TF}(x) \cdot \mathbf{n}_{TF}]^- \varphi_i(x)\varphi_j(x)$
      end for
      for each basis function $\varphi_j \in \mathcal{B}_T^k$ **do**
        $A_{\varphi_i,\varphi_j} \leftarrow A_{\varphi_i,\varphi_j} + w_x [\mathrm{U}_{TF}(x) \cdot \mathbf{n}_{TF}]^- \varphi_i(x)\varphi_j(x)$
      end for
    end for
    for each basis function $\varphi_i \in \mathcal{B}_F^k$ **do**
      for each basis function $\varphi_j \in \mathcal{B}_F^k$ **do**
        $A_{\varphi_i,\varphi_j} \leftarrow A_{\varphi_i,\varphi_j} + w_x [\mathrm{U}_{TF}(x) \cdot \mathbf{n}_{TF}]^- \varphi_i(x)\varphi_j(x)$
      end for
    end for
  end for
end for

Algorithm 8 Assembly of the concentration source vector.

Set $\boldsymbol{b}_{\varphi_i} = 0$ for all $\varphi_i \in \mathcal{B}_T^k$
for each edge $F \in F_T$ **do**
  for each quadrature node (x, w_x) of K_{TF} **do**
    for each basis function $\varphi_i \in \mathcal{B}_T^k$ **do**
      $b_{\varphi_i} \leftarrow b_{\varphi_i} + w_x \varphi_i(x)(q^+(t^{n+1/2}, x)\hat{c}(t^{n+1/2}, x) + \frac{2\Phi}{\Delta t} \mathrm{c}_h^n(x))$
    end for
  end for
end for

Acknowledgments. The authors would like to thank Daniele Di Pietro and Matteo Cicuttin for giving us access to the hho software platform,[1] which served as an invaluable starting point for our implementation.

REFERENCES

[1] Y. Amirat and A. Ziani, *Asymptotic behavior of the solutions of an elliptic-parabolic system arising in flow in porous media*, Z. Anal. Anwend., 23 (2004), pp. 335–351.
[2] S. Bartels, M. Jensen, and R. Müller, *Discontinuous Galerkin finite element convergence for incompressible miscible displacement problems of low regularity*, SIAM J. Numer. Anal., 47 (2009), pp. 3720–3743, https://doi.org/10.1137/070712079.
[3] F. Bassi, L. Botti, A. Colombo, D. A. Di Pietro, and P. Tesini, *On the flexibility of agglomeration based physical space discontinuous Galerkin discretizations*, J. Comput. Phys., 231 (2012), pp. 45–65, https://doi.org/10.1016/j.jcp.2011.08.018.
[4] L. Beirão da Veiga, F. Brezzi, A. Cangiani, G. Manzini, L. D. Marini, and A. Russo, *Basic principles of virtual element methods*, Math. Models Methods Appl. Sci., 199 (2013), pp. 199–214.
[5] L. Beirão da Veiga, J. Droniou, and G. Manzini, *A unified approach for handling convection terms in finite volumes and mimetic discretization methods for elliptic problems*, IMA J. Numer. Anal., 31 (2011), pp. 1357–1401, https://doi.org/10.1093/imanum/drq018.
[6] F. Brezzi, K. Lipnikov, and M. Shashkov, *Convergence of the mimetic finite difference method for diffusion problems on polyhedral meshes*, SIAM J. Numer. Anal., 43 (2005), pp. 1872–1896, https://doi.org/10.1137/040613950.
[7] C. Chainais-Hillairet and J. Droniou, *Convergence analysis of a mixed finite volume scheme for an elliptic-parabolic system modeling miscible fluid flows in porous media*, SIAM J. Numer. Anal., 45 (2007), pp. 2228–2258.
[8] C. Chainais-Hillairet, S. Krell, and A. Mouton, *Study of discrete duality finite volume schemes for the Peaceman model*, SIAM J. Sci. Comput., 35 (2013), pp. A2928–A2952, https://doi.org/10.1137/130910555.
[9] C. Chainais-Hillairet, S. Krell, and A. Mouton, *Convergence analysis of a DDFV scheme for a system describing miscible fluid flows in porous media*, Numer. Methods Partial Differential Equations, 31 (2015), pp. 723–760, https://doi.org/10.1002/num.21913.
[10] Z. Chen and R. Ewing, *Mathematical analysis for reservoir models*, SIAM J. Math. Anal., 30 (1999), pp. 431–453.
[11] M. Cicuttin, D. D. Pietro, and A. Ern, *Implementation of discontinuous skeletal methods on arbitrary-dimensional, polytopal meshes using generic programming*, J. Comput. Appl. Math., 2017, https://doi.org/10.1016/j.cam.2017.09.017.
[12] B. Cockburn, D. A. Di Pietro, and A. Ern, *Bridging the hybrid high-order and hybridizable discontinuous Galerkin methods*, ESAIM Math. Model. Numer. Anal., 50 (2016), pp. 635–650.
[13] D. Di Pietro and S. Lemaire, *An extension of the Crouzeix–Raviart space to general meshes with application to quasi-incompressible linear elasticity and stokes flow*, Math. Comp., 84 (2015), pp. 1–31.
[14] D. A. Di Pietro, *private communication*, 2017.

[1] *Agence pour la Protection des Programmes* deposit IDDN.FR.001.220005.000.S.P.2016.000.10800.

[15] D. A. Di Pietro, J. Droniou, and A. Ern, *A discontinuous-skeletal method for advection-diffusion-reaction on general meshes*, SIAM J. Numer. Anal., 53 (2015), pp. 2135–2157.
[16] D. A. Di Pietro and A. Ern, *Mathematical Aspects of Discontinuous Galerkin Methods*, Math. Appl. 69, Springer, New York, 2011.
[17] D. A. Di Pietro and A. Ern, *Hybrid high-order methods for variable-diffusion problems on general meshes*, C. R. Math., 353 (2015), pp. 31–34.
[18] D. A. Di Pietro, A. Ern, and S. Lemaire, *An arbitrary-order and compact-stencil discretization of diffusion on general meshes based on local reconstruction operators*, Comput. Methods Appl. Math., 14 (2014), pp. 461–472.
[19] J. Droniou, *Finite volume schemes for diffusion equations: Introduction to and review of modern methods*, Math. Models Methods Appl. Sci., 24 (2014), pp. 1575–1619.
[20] J. Droniou and R. Eymard, *A mixed finite volume scheme for anisotropic diffusion problems on any grid*, Numer. Math., 105 (2006), pp. 35–71.
[21] J. Droniou, R. Eymard, T. Gallouët, and R. Herbin, *A unified approach to mimetic finite difference, hybrid finite volume and mixed finite volume methods*, Math. Models Methods Appl. Sci., 20 (2010), pp. 265–295, https://doi.org/10.1142/S0218202510004222.
[22] J. Droniou and K. S. Talbot, *On a miscible displacement model in porous media flow with measure data*, SIAM J. Math. Anal., 46 (2014), pp. 3158–3175.
[23] J. Droniou and K. S. Talbot, *Analysis of miscible displacement through porous media with vanishing molecular diffusion and singular wells*, Ann. Inst. H. Poincaré Anal. Non Linéaire, accepted, arXiv:1609.03244, 2017.
[24] D. A. Dunavant, *High degree efficient symmetrical Gaussian quadrature rules for the triangle*, Internat. J. Numer. Methods Engrg., 21 (1985), pp. 1129–1148.
[25] R. E. Ewing, *The Mathematics of Reservoir Simulation*, Vol. 1, SIAM, Philadelphia, 1983.
[26] R. E. Ewing, T. F. Russell, and M. F. Wheeler, *Simulation of miscible displacement using mixed methods and a modified method of characteristics*, in Proceedings of the SPE Reservoir Simulation Symposium, Society of Petroleum Engineers, 1983.
[27] R. E. Ewing, T. F. Russell, and M. F. Wheeler, *Convergence analysis of an approximation of miscible displacement in porous media by mixed finite elements and a modified method of characteristics*, Comput. Methods Appl. Mech. Engrg., 47 (1984), pp. 73–92.
[28] R. Eymard, T. Gallouët, and R. Herbin, *Discretization of heterogeneous and anisotropic diffusion problems on general nonconforming meshes SUSHI: A scheme using stabilization and hybrid interfaces*, IMA J. Numer. Anal., 30 (2010), pp. 1009–1043.
[29] X. Feng, *On existence and uniqueness results for a coupled system modeling miscible displacement in porous media*, J. Math. Anal. Appl., 194 (1995), pp. 883–910.
[30] R. Herbin and F. Hubert, *Benchmark on Discretization Schemes for Anisotropic Diffusion Problems on General Grids*, in Finite Volumes for Complex Applications V, Wiley, New York, 2008, pp. 659–692.
[31] J. G. Heywood and R. Rannacher, *Finite-element approximation of the nonstationary Navier–Stokes problem.* IV. *Error analysis for second-order time discretization*, SIAM J. Numer. Anal., 27 (1990), pp. 353–384, https://doi.org/10.1137/0727022.
[32] E. J. Koval, *A method for predicting the performance of unstable miscible displacement in heterogeneous media*, Soc. Petrol. Eng. J., 3 (1963), pp. 145–154.
[33] R. J. LeVeque, *Finite Difference Methods for Ordinary and Partial Differential Equations: Steady-State and Time-Dependent Problems*, Clasics Appl. Math. 98, SIAM, Philadelphia, 2007.
[34] B. Li and W. Sun, *Regularity of the diffusion-dispersion tensor and error analysis of Galerkin FEMs for a porous medium flow*, SIAM J. Numer. Anal., 53 (2015), pp. 1418–1437, https://doi.org/10.1137/140958803.
[35] K. Lipnikov and G. Manzini, *A high-order mimetic method on unstructured polyhedral meshes for the diffusion equation*, J. Comput. Phys., 272 (2014), pp. 360–385, https://doi.org/10.1016/j.jcp.2014.04.021.
[36] D. W. Peaceman, *Improved treatment of dispersion in numerical calculation of multidimensional miscible displacement*, Soc. Petrol. Eng. J., 6 (1966), pp. 213–216.
[37] D. W. Peaceman and H. H. Rachford, Jr., *Numerical calculation of multidimensional miscible displacement*, Soc. Petrol. Eng. J., 2 (1962), pp. 327–339.
[38] H. Wang, *An optimal-order error estimate for an ELLAM scheme for two-dimensional linear advection-diffusion equations*, SIAM J. Numer. Anal., 37 (2000), pp. 1338–1368.
[39] H. Wang, *An optimal-order error estimate for a family of ELLAM-MFEM approximations to porous medium flow*, SIAM J. Numer. Anal., 46 (2008), pp. 2133–2152.

[40] H. Wang, D. Liang, R. E. Ewing, S. L. Lyons, and G. Qin, *An approximation to miscible fluid flows in porous media with point sources and sinks by an Eulerian–Lagrangian localized adjoint method and mixed finite element methods*, SIAM J. Sci. Comput., 22 (2000), pp. 561–581.

[41] H. Wang, D. Liang, R. E. Ewing, S. L. Lyons, and G. Qin, *An ELLAM-MFEM solution technique for compressible fluid flows in porous media with point sources and sinks*, J. Comput. Phys., 159 (2000), pp. 344–376, https://doi.org/10.1006/jcph.2000.6450.